Fermi National Accelerator Laboratory

FERMILAB-Pub-82/39-THY
June, 1982

Phase Structure and Renormalization Trajectories of Lattice SU(2) Gauge Theory

KHALIL M. BITAR,[a] STEVEN GOTTLIEB,[b] and COSMAS K. ZACHOS
Fermi National Accelerator Laboratory, Batavia, Illinois 60510

(Received

ABSTRACT

We indicate how the phase diagrams of lattice gauge theories are easily obtainable through real space renormalization techniques of the Migdal-Kadanoff transform type. As an illustration, we work out the phase boundaries for an SU(2) single plaquette action with variable components of spin 1/2 (the Wilson form), spin 1 (SO(3)), and spin 3/2. In this three-dimensional space, we study the renormalization flows for the couplings, thereby determining the infrared stable forms of the action. We discuss their dependence on the phase boundary and their import to the continuum limit of the lattice theory.

PACS numbers: 11.15.Ha, 11.10.Gh, 64.60.-i.

[a] On leave of absence from the American University of Beirut, Lebanon.

[b] Address as of September 1982: UCSD, La Jolla, CA. 92093

I. INTRODUCTION

The extraction of physical information from lattice gauge theories is complicated by the nontrivial phase structure recently observed in the space of alternative actions. Specifically, without altering the naive continuum limit of the theory, one may define single plaquette actions which contain varying components of the Wilson action (i.e. the trace of the fundamental representation of the gauge group) as well as additional higher representations. For the SU(2) gauge theory, Bhanot and Creutz[1] have observed through Monte Carlo techniques an interesting first order phase boundary in the space spanned by the Wilson action and the adjoint action [SO(3)]. They have also noticed an alarming variability of Λ_{lattice}, emphasized and discussed in further papers.[3,4]

There is another method for establishing the phase structure of alternative actions, which, unlike Monte Carlo, addresses the significance of the phase boundaries to the renormalization process, by its very nature. In addition, it is not inherently limited by finite lattice sizes. The method relies on the real space renormalization group transformations proposed by Migdal[5] and extended by Kadanoff,[6] and Martinelli and Parisi.[7] The renormalization recursions available so far are inexact for more than two spacetime dimensions: they project the effective action relevant to a larger scale lattice obtained by each recursion onto the space of single plaquette actions. Even though the most general plaquette action is accommodated in that space, the nonlocal terms induced in the renormalization process[8] cannot be included without drastic losses in computability.[7]

In this paper, we point out that the Migdal recursion technique, even though it is known to miss the order of the phase transition investigated in most cases, [5,6,7,9] provides a fast and efficient method to obtain the critical couplings, and hence the phase diagrams in which one is interested. Because these phase diagrams can be obtained with a small fraction of the computer time required for a Monte Carlo study of the same action, it is possible to study alternative actions of greater complexity. We illustrate this by particularizing to the SU(2) lattice pure gauge theory in the space spanned by a Wilson action component (spin 1/2), an adjoint component (spin 1), and a spin 3/2 component, parameterized by their relative inverse couplings $\beta_F \equiv \beta c_F$, $\beta_A \equiv \beta c_A$, and $\beta_3 \equiv \beta c_3$, respectively. We have been considerably aided in our analysis by the study of the pure Wilson theory through this technique by Nauenberg and Toussaint[9] (also see Ref. 10).

After iterating the renormalization recursions a large number of times to find the effective single plaquette action pertaining to a lattice with correspondingly larger spacing, we can perform the functional integral to a good approximation (Sec. II). Having thus obtained the free energy density, we may differentiate with respect to the appropriate inverse coupling β to obtain the intensive thermodynamic functions of the theory, like the energy and the heat capacity. Identifying the location of the heat capacity peak with the critical coupling β_c, we obtain the phase boundaries for the positive β_F, β_A, β_3 octant of the manifold studied here (Fig 1).

In the β_F-β_A subspace of that diagram, it is rewarding to find striking agreement with the Monte Carlo results for that region[1] (Fig. 5). The extended phase boundary is a roughly flat surface

which connects this boundary to a similar structure we find in the β_A-β_3 subspace (Fig. 6). Several of its interesting features are conveniently located through an analysis of the single plaquette classical minima (SPCM) for the action (Appendix A). We find that, in agreement with the observation of Bachas and Dashen,[11] some of these phase transition features appear not to be underlied in any way by the center Z_2 of the group.

As mentioned, the correct order of the phase transition cannot be established by the Migdal technique. (In fact, part of the first order phase boundary is seen here as third order.) Thus, in general, such a study of a phase boundary can be usefully supplemented by very few Monte Carlo runs.

Since the method discussed relies on the renormalization process of the single plaquette action, it is relatively easy to monitor the evolution of the effective action with increasing lattice spacings (Sec. 4). We do this by fitting its functional form to components of spin 1/2, 1, 3/2, and 2, the last one serving as an indicator of the degree to which the effective action has "leaked out" of the space in which it was defined.

We find very little leakage, with some special exceptions. All renormalization trajectories of the couplings avoid the phase boundaries and terminate at the origin $\beta_F=\beta_A=\beta_3=\beta_2=0$ (Fig. 8). However, if they happen to start from regions separated from the origin by phase boundaries (e.g. WVX in Fig.1), they do not cross them. Instead, they develop a comparatively large component of spin 2 (and perhaps higher spins), and approach the origin through a window, which appears to be present in the manifold which includes spin 2 or higher.

A similar, more standard, approach to the origin through a phase boundary window which we have mapped out is evident in Fig. 8. It can be seen that, regardless of their point of origin, the trajectories are attracted to and eventually coalesce with either of two stable fixed lines. These lines are located along the SO(3) axis β_A, and, more usually, the Wilson action axis β_F, with a 16% negative component of β_A, respectively. In addition to representing the universal limit for long distances of the various bare alternative actions defined on a lattice with very small spacing, these universal fixed lines suggest the path of fastest approach to the continuum limit, since they appear to exhibit markedly improved scaling behavior, in comparison to other trajectories with even smaller continuum couplings (Sec. V).

A brief discussion of alternative recursion formulas and lattice spacing increments is provided in Appendix B.

II. DESCRIPTION OF THE MIGDAL RECURSION TECHNIQUE

We briefly review the Migdal transformation formalism. To the extent convenient, we try to align our notations and conventions with those of Nauenberg and Toussaint[9] who study SU(2) with a Wilson action in somewhat greater detail than Migdal's original treatment.[5]

The central object studied is the functional integral of a euclidean lattice gauge theory:

$$Z = \int [dU_{link}] \; e^{-\sum_p S_p(U_p, a)} \tag{2.1}$$

where U_p denotes the product of U_{link}'s along the perimeter of the plaquette and a is the lattice spacing.

The gauge invariant one plaquette action $S_p(U,a)$ is a class function, i.e. it does not depend on the degrees of freedom of U which can be "gauged" away: it is completely determined by those specifying the equivalence class of U. A complete expansion basis for a general class function is the set of characters of the group. The character $\chi_r(U)$ is the trace of U in the irreducible representation indexed by r. Since U is unitarily diagonalizable, the character is the sum of its eigenvalues. The dimensionality of the representation is $d_r = \chi_r(1)$. The identity (singlet) representation is denoted by r = 0.

Given a group invariant integration measure, dV, normalized so that $\int dV = 1$, the complete set of characters constitutes an orthonormal basis by virtue of the relation:

$$\int dV\ \chi_r(UV)\,\chi_s^*(W^\dagger V) = \frac{\delta_{rs}}{d_r}\,\chi_r(UW)\ , \qquad (2.2)$$

analogous to the orthonormality relation for finite groups. We thus character expand the exponential of the single plaquette action:

$$e^{-S_p(U,a)} = \sum_r F_r(a)\ d_r\ \chi_r(U) \qquad (2.3)$$

$$F_r(a) = \frac{1}{d_r}\int dU\ e^{-S_p(U,a)}\chi_r^*(U) \qquad (2.4)$$

If one decimated a number of the links in (2. 1) by performing the group integrals over the appropriate links so as to end up also with a hypercubic lattice, the resulting exact effective action would not, in general, be describable in terms of a sum over single plaquettes.

However, Migdal[5] has proposed the following renormalization which yields an effective single plaquette action $S_p(U,\lambda a)$ - in general different from $S_p(U,a)$ - on a lattice whose spacing is scaled up by a factor λ (not necessarily integral). For more than two spacetime dimensions, the transformation is inexact, since it does not generate interactions more complex than the general single plaquette interaction.[5-8] Nonetheless, it is believed to preserve the essential features of the dynamics of the system. It reads:

$$e^{-S_p(U,\lambda a)} = \left[\sum_r F_r(a)\lambda^2 d_r \chi_r(U)\right]^{\lambda^{d-2}} \qquad (2.5)$$

d is the dimensionality of spacetime; for d = 2 the transformation is exact. Motivation and assessment of the performance of this transformation and its variants are discussed in Appendix B. We find below that it provides a fast and efficient heuristic description of the system.

Migdal's transformation (2.5) reduces to the identity for $\lambda = 1$, as it should, and, in practice, two successive transformations by λ are not precisely equivalent to one by λ^2. Upon N iterative transformations of this kind performed numerically, we may monitor the evolution of the functional form of $S_p(U,\lambda^N a)$ and thus study the renormalization of the action with an increase of scale. This we do in Sec. IV.

After a large number of tranformations, volume effects in each cell overwhelm boundary effects - the integral (2.1) virtually factorizes, so that each large plaquette may be readily integrated over independently of its neighboring ones. The free energy per plaquette is then

$$\mathcal{F} = \lim_{N\to\infty} \mathcal{F}_N \quad \text{, where} \quad \mathcal{F}_N = \frac{1}{\lambda^{Nd}} \ln F_{r=0}(\lambda^N a) \tag{2.6}$$

From the computational standpoint, when iterating (2.5) numerically, we wish to avoid taking logarithims of very large or very small numbers in (2.6). To this end, we normalize after every iteration, following Ref. 9

$$C_r(a) \equiv F_r(a) \Big/ e^{-S_p(\mathbb{1},a)} \tag{2.7}$$

$$R(U,a) \equiv \sum_r C_r \lambda^2 d_r \chi_r(U) = e^{-\lambda^{2-d} S(U,\lambda a) + \lambda^2 S(\mathbb{1},a)} \tag{2.8}$$

$$\mathcal{F}_N = -S_p(\mathbb{1},a) + \frac{1}{\lambda^2} \sum_{m=0}^{N-1} \frac{1}{\lambda^{md}} \ln R(\mathbb{1},\lambda^m a) + \frac{1}{\lambda^{Nd}} \ln C_0(\lambda^N a) \tag{2.9}$$

which converges rapidly in N.

We proceed to apply this formalism to SU(2). In SU(2), the characters are all real and the representation index is just the spin. Since the rank of the group is 1, they depend on only one angle θ (corresponding to the azimuth ϕ of the L_z eigenfunctions). An arbitrary element U of SU(2) is unitarily diagonalizable to a (2r+1)x(2r+1) unimodular matrix whose eigenvalues sum to:

$$\chi_r(U) = e^{i\theta r} + e^{i\theta(r-1)} + \cdots + e^{-i\theta(r-1)} + e^{-i\theta r} = \frac{\sin(2r+1)\theta/2}{\sin\theta/2}$$

$$(r = 0, \tfrac{1}{2}, 1, \tfrac{3}{2}, \ldots) \qquad d_r = \chi_r(\mathbb{1}) = 2r+1 \tag{2.10}$$

Even in the absence of the above closed form (as would be the case for higher groups) the character of the fundamental representation $\chi_{1/2}(U) = 2\cos\theta/2$ may be Kronecker-multiplied with itself to decompose into the standard sums of all higher irreducible representations (addition of angular momenta). Naturally, all such character identities reduce to the dimensionality formulas at the identity ($U=\mathbb{1}$, i.e. $\theta=0$):

$$\chi_1(U) = \chi_{1/2}(U)\cdot\chi_{1/2}(U) - \chi_0(U) = 2\cos\theta + 1$$

$$\chi_{3/2}(U) = \chi_{1/2}(U)\cdot\chi_1(U) - \chi_{1/2}(U) = 2(\cos 3\theta/2 + \cos\theta/2)$$
$$= 4\cos\theta\cos\theta/2$$

$$\chi_2(U) = \chi_{3/2}(U)\cdot\chi_{1/2}(U) - \chi_1(U) =$$

$$= 2\cos 2\theta + 2\cos\theta + 1 \qquad (2.11)$$

, etc....

In this paper we will restrict ourselves to an initial single plaquette action consisting of linear combinations of spin 1/2 (Wilson form), spin 1 [the SO(3) action], and spin 3/2, parameterized as follows:

$$S_p = -\left[\beta_F (\chi_{1/2}(U) - 2) + \beta_A (\chi_1(U) - 3) + \beta_3 (\chi_{3/2}(U) - 4)\right] \quad (2.12)$$

We may further suppress the overall constant normalization terms, since shifting the plaquette action by a constant does not affect the specific heat we will be computing:*

$$-S_p(\theta, a) = 2\left[\beta_F \cos\theta/2 + \beta_A \cos\theta + 2\beta_3 \cos\theta \cos\theta/2\right] \equiv$$

$$\equiv 2\beta\left[c_F \cos\theta/2 + c_A \cos\theta + 2c_3 \cos\theta \cos\theta/2\right]$$

(2.13)

The bare coupling of the continuum field theory is read off from the coefficient of the θ^2 in the above action (θ^2 is proportional to the trace of the field strength squared):

$$\frac{1}{g_0^2} = \frac{\beta_F}{2} + 2\beta_A + 5\beta_3 \quad (2.14)$$

---

*Note that our couplings are normalized differently from Ref. 1 and Ref. 3, i.e.

$$\beta_F = \frac{1}{2}\beta_F^{\text{Creutz}} = \frac{1}{2}\beta_F^{\text{Pashen}}, \quad \beta_A = \frac{1}{3}\beta_A^{\text{Creutz}} = \frac{1}{4}\beta_A^{\text{Pashen}}$$

The Haar measure in this parameterization is:

$$\int [dU] = \int_0^{4\pi} \frac{d\theta}{2\pi} \sin^2\left(\frac{\theta}{2}\right) \qquad (2.15)$$

so that the character ("Fourier") coefficients (2.4) are readily given by:

$$F_r(\lambda^N a) = \frac{1}{(2r+1)2\pi} \int_0^{4\pi} d\theta \sin^2\theta/2 \; e^{-S(\theta,\lambda^N a)} \chi_r(\theta) \qquad (2.16)$$

The reader may note that this measure identifies the $\chi_r(\theta)$ with the (hyperspherical) Gegenbauer polynomials $C^1_{2r}(\cos\theta/2)$.

We may thus compute the dependence of the family of functions $S(\theta,\lambda^N a)$ on N, given a triplet of values $(\beta_F,\beta_A,\beta_3) \equiv \beta(c_F,c_A,c_3)$. In the large N limit we obtain the free energy density $\mathcal{F}(\beta)$(2.6). We may then take successive derivatives with respect to β, to obtain the average plaquette action $\langle S_p/\beta \rangle$ and its variance, the specific heat C:

$$-\left\langle \frac{S_p}{\beta} \right\rangle = \frac{\partial \mathcal{F}}{\partial \beta} = \left\langle 2c_F \cos\theta/2 + 2c_A \cos\theta + 4c_3 \cos\theta \cos\theta/2 \right\rangle \qquad (2.17)$$

$$C = \beta^2 \frac{\partial^2 \mathcal{F}}{\partial^2 \beta^2} = \left(\langle S_p^2 \rangle - \langle S_p \rangle^2 \right) \qquad (2.18)$$

Note that C is independent of the absolute normalization of β. In a first order phase transition $C(\beta)$ should be singular like a δ-function at β_c, while it should be discontinuous in a second order transition, its slope should be discontinuous in a third order transition, etc. We study $C(\beta)$ for several values of (c_F,c_A,c_3) with special attention to such structure.

III. THE PHASE STRUCTURE OF SU(2) IN A THREE DIMENSIONAL SPACE OF ACTIONS

Starting with the action (2.13), we perform a number of Migdal transformations until $\mathcal{F}_N$ converges to a constant. we take $\lambda = 1.1$, which is a priori reasonable since it reproduces the known[13] critical coupling of the SO(3) phase transition fairly well (V on Fig. 1). In Appendix B we discuss the variability of our results with λ or with using alternative recursion formulas. We keep 20 characters in the expansion (2.3), since we have not encountered nozero coefficients for $r \geq 20$. Convergence takes typically from 20 to 150 iterations, corresponding to scaling up by a factor $\lambda^{20}=6.7$ to $\lambda^{150}=1.6\times10^{6}$, respectively, depending on the point $\vec{\beta}\equiv\beta\vec{c}\equiv\beta(c_F,c_A,c_3)$ studied.

We run along rays of fixed $\vec{c} \equiv (c_F,c_A,c_3)$, varying β sequentially by $\Delta\beta = .01$ to obtain $\mathcal{F}(\beta)$. We then differentiate once to obtain the average plaquette action (2.17), and once more to obtain the heat capacity $C_{(\beta)}$(2.18). Sample shapes of these curves are provided in Figs. 2, 3, 4. Although the phase transitions on the $(c_F,c_A,0)$ are known to be first order from Monte Carlo[1] studies, we find no discontinuities in the average plaquette action; this comes as no surprise, since, due perhaps to the implicit averaging of links involved, the Migdal technique is known to often miss the correct order of a given phase transition.[5,6,7,9] In fact, the most singular behavior observed in our study has been cusps in the specific heat which, taken at face value, would signal a third order phase transition. Nevertheless, as also observed in the past,[5,6] the critical coupling of a phase transition is predicted fairly accurately through the Migdal

technique: the centers of the $\vec{c}$ peaks on the $(c_F, c_A, 0)$ plane fall remarkably close to the phase boundary established by Monte Carlo techniques - see Fig. 5.

We thus perform 46 radial runs whose results are given in Table 1. We indicate the location of the $\vec{c}$ peak, its height, and its shape (i.e. whether it is a cusp: x, a peak: o, or a very wide bump: U. A slash: / separates two peaks on the same radial run (see Fig. 4). (In two runs the peak required by continuity from nearby points falls outside our running range.)

On the basis of the regularities of our results and some theoretical guidelines provided by considerations of Single Plaquette Classical Minima[11] (SPCM, see Appendix A), we have chosen our points to cover the regions that appear to have the most interesting structure. The phase boundary in the octant studied emerges as on Fig. 1, which we proceed to describe and discuss.

The 18 runs performed in the β_F-β_A plane reproduce the SO(3) - SU(2) phase diagram (Fig. 5) already available from Monte Carlo studies.[1] As the slope c_A/c_F is increased, the very wide, low bumps turn into higher narrow peaks (Fig. 4) - the highest one is at $\vec{\beta}$ = (.35,.69,0). Although we observe a swift narrowing of the peaks from $\vec{c}$ = (1,.25, 0) to $\vec{c}$ = (1, .30, 0), we cannot locate the critical endpoint as precisely as the Monte Carlo study:[1] $\vec{\beta}$ = (0.74,0.30,0). In any case, by comparison to this study, we will be interpreting wide bumps (U) of this type to signal the absence of a phase boundary, while the peaks (o) and cusps (x) will be interpreted to demarcate a first order boundary.

With increasing slope, we observe the peak separating itself past the triple point W: $\vec{\beta}$ = (.29,.79,0) into a peak and a cusp (Fig. 4). This bifurcation of the phase boundary is dictated by consistency with the well known SO(3) phase transition[13] V on the β_A axis, and the Z_2 transition Q, at the self-duality value $\beta_F = 2.22$[5,14] and sufficiently large β_A. Large β_A freezes out all degrees of freedom except those in the center Z_2, viz. $U = \pm\mathbb{1} \Rightarrow \theta = 4\pi, 2\pi, 0$.

Following Bachas and Dashen[11] we observe that the window in the phase boundary is almost exactly in that region of the plane (BOF) in which there are no nontrivial SPCM's - see Appendix A. To the left of OB there is alays one minimum in addition to the vacuum, corresponding to the center element $U = -\mathbb{1}$.

A similar diagram is also obtained through the 10 runs covering the β_3-β_A plane (Fig. 6). The peak-cusp structure for larger β_A is analogous to that observed on the β_F-β_A plane, with the Z_2 phase transition R appropriately scaled downto $\beta_3 \simeq 1.11$ for large β_A, due to our normalization (2.13).

In contrast to the previous triple point W, the triple point X≃(0,.76,.40) essentially lies on the SPCM line EO ($\beta_A = 2.5\ \beta_3$). Significantly, to the left of this line the SPCM's lie in the center Z_2 - this region includes the Z_2 phase transition R - while to the right of it, the nontrivial SPCM's cease to lie in the center Z_2. This may also account for the fact that past the triple point the phase boundary is demarcated by cusps of increasing height and continues uninterrupted to the β_3 axis. T has, in fact, the highest cusp observed in our study. The reader may wish to contrast this to the point S on the β_F axis, where no nontrivial SPCM's exist.

The diagram on the β_F-β_3 plane (Fig. 7) is considerably simpler, possibly due to the absence of any underlying Z_2 structure. We observe the phase boundary TU demarcated by cusps to terminate on, or near, the SPCM boundary OD ($\beta_3 = .50\ \beta_F$); for higher slopes there are no other minima except for the vacuum. In the window SU the cusps turn to peaks of decreasing height/increasing width and then rapidly into low, wide bumps of the type identified above to signal the absence of a phase boundary.

Given these intersections of the phase boundary surface with the three planes $\beta_3=0, \beta_F=0$, and $\beta_A=0$, we perform 13 more runs to obtain a consistent picture of this surface (Fig. 1). The surface appears fairly flat (roughly $\beta_A+\beta_F+\beta_3\simeq 1$) except for the structure attendant to Z_2 to the left of the SPCM plane EOB. This plane intersects the surface along XYZ, while the SPCM region which contains no nontrivial minima intersects the surface along UYZS (see Appendix A).

The region YXTU (which is presumably not controlled by Z_2) is characterized by cusps. The window enclosed by UYZS contains very wide bumps and we therefore do not regard it as a phase boundary. The region XZW is typified by narrow peaks and lies within the SPCM region dominated by the center. The reader may wish to contrast the ray $\vec{c} =$ (2,1.30,.40) which has a sharp cusp and lies outside the window UYZS, to the rays (2,1,0.5), (2,0.5,0.03), and (1,.10,.10) which lie inside this window and exhibit a peak and very wide bumps respectively (Table I).

The region XZW continues down to WXV, which is also characterized by peaks. The surface XZW interfaces with the surface QRXW along the flat curve WX; the latter surface is characterized by cusps and connects to the Z_2 phase transition.

Finally, motivated by the trajectories dicussed in the next section, we ran along the ray (1,-.10,.02) which is very close to the major infrared attractive fixed line of actions; the heat capacity is extraordinarily flat, with a bump barely discernible. Perhaps significantly, the elevation of this bump is the lowest in the entire diagram. In this connection, we point out to the reader that the only other local minimum in the height of C in our octant is located on the β_A axis, i.e. close to the minor [SO(3)] fixed line of actions.

The technique illustrated here could be easily extended to study the three other octants of the space discussed whose structure is not identical to the one investigated; the remaining four are connected to these by the symmetry: $\beta_A \to \beta_A, \beta_F \to -\beta_F, \beta_3 \to -\beta_3$.

IV. THE RENORMALIZATION TRAJECTORIES OF THE COUPLINGS

In order to read off the thermodynamic functions in the previous section, points in the $(\beta_F, \beta_A, \beta_3)$space of actions were chosen and then the equivalent single plaquette action system on a lattice with spacing $\lambda^N a$ was obtained through N successive renormalization transformations. As the scale of the spacing expands, the single plaquette action $S_p(\theta, \lambda^N a)$ differs from the original one $S_p(\theta, a)$. Not only do the renormalized inverse couplings β ultimately decrease, but the functional form iself of the action $S_p(\theta)$ varies with N, as a consequence of the additional interactions introduced by the renormalization process.

We monitor this evolution of $S_p(\theta)$ as follows. Every few iterations (2 or 5) we fit $\exp(-S_p(\theta, \lambda^N a) + S_p(0, \lambda^N a))$ with the four-parameter family of functions

$$e^{\beta_F(\chi_{1/2}(\theta)-2)+\beta_A(\chi_1(\theta)-3)+\beta_3(\chi_{3/2}(\theta)-4)+\beta_4(\chi_2(\theta)-5)} \tag{4.1}$$

through the fitting program MINUIT. Our periodic viewing of the values $\beta_F,\beta_A,\beta_3,\beta_4$ which best describe the effective action of the system does not interfere with the operation of the iteration process or alter the renormalization of the action in any way.

Of all the higher spins which are in general generated through the renormalization process, we only choose to read off the spin 2 component, which we parameterize by β_4. In most cases (with a few notable exceptions) it is relatively very small and it may serve as a crude indicator of the amount of the action which "leaks" out of the three dimensional space $(\beta_F,\beta_A,\beta_3)$ in which we start.

Table II provides the sequence of inverse couplings for 4 out of the 25 sample trajectories studied. With the apparent exception of the last one, all trajectories in the table avoid phase boundaries, and to this end sometimes temporarily increase their distance from the origin while curving around to flow to the origin through the "window" on the phase boundary below Z. They are all attracted to a line which represents a one parameter family of actions, that is, a universal functional form (close to the form of the Wilson action), along which they flow to the origin.[5-9]

The last trajectory in Table II starts on the adjoint axis and is separated from the origin by the phase boundary VW in the $\beta_F,\beta_A,\beta_3>0$ octant. Since half integral spins cannot be produced from spin 1, symmetry should constrain every other character to be zero. We could thus expect to interpret the β_F,β_3 components (which are always $<.02$) as

a rough indication of the aggregate error in our iteration procedure and the fitting routine. (Even this trajectory does not cross the phase boundary: instead it rapidly develops a spin 2 component (and possibly higher ones) and it "leaks" through a window in spin 2 and/or higher spins. Even though we have not studied the continuation of the phase diagram to the space of higher spins, a window in the β_A-β_4 plane is not implausible, given the absence of a Z_2 phase transition and the boundary connecting to it.) We further find that within a smaller region around the adjoint axis β_A, all trajectories are attracted to another [SO(3)] stable line very close to that axis.

In Fig. 8 we plot the evolution of the two dominant components β_F and β_A for several trajectories starting from points on the β_F-β_A plane - the components β_3 and β_4 are usually smaller by at least one order of magnitude. The plot illustrates the basic pattern observed in all our runs.

Trajectories curl around and avoid the phase boundary by going through the window below the endpoint Z (or as is the case for the trajectory starting at β_F=.1, β_A=.9, the window for $\beta_F\simeq 0$, nontrivial β_4, $\beta_A\simeq$.8, not depicted here). Their approach to the origin is eventually along the universal stable lines which lie very close to the β_F and the β_A axes, respectively. The major [SU(2)] stable line is not entirely straight and has an approximate slope of -.16. We illustrate this on Fig. 9, on which the β_A and β_3 components of three trajectories are scaled up by one order of magnitude. This plot of couplings versus iteration number indicates how trajectories coalesce to the stable line. Observe that the shape of the sequence of β_F coefficients is somewhat different from that of the β_Ax10 sequence, i.e. the stable line is not exactly

straight for strong coupling (small β. See Ref. 8).

We may observe that, very qualitatively, the trajectories appear to flow to regions of decreasing heat capacity C. Although we could not establish the precise relation of C to a potential of a gradient flow for the couplings, it still appears significant that the doubly unstable point on the β_A-β_F plane (i.e. that point to which no trajectory flows) seems to be located near the highest C peak found on this plane: at $\beta_F \simeq .33$, $\beta_A \simeq .72$, in the neighborhood of the triple point W. If a line were drawn between that point and the origin, it would, together with the phase boundary QW, divide the plane into two regions. The trajectories in the right and left regions eventually join the SU(2) and the SO(3) stable lines respectively. As remarked in the last section, both of these fixed lines go through "valleys," i.e. regions with lowest heat capacity peaks.

All trajectories we have studied which start from points on the octant of Fig. 1 outside the shaded phase boundary eventually curve around in occasionally large arcs and reach the origin along the major SU(2) stable line. For instance, the third trajectory in Table II, a portion of which is plotted in Fig. 1, starts with $\beta_F=0$. It rapidly develops a large β_F component, curves around near (8.6, -1.1, -.7), and flows to the origin with slope $\sim$ -.18 to -.16. We discuss the significance of these trajectories in the next section.

V. DISCUSSION AND CONCLUSIONS

We have illustrated (in Sec. III) how the phase boundary of a gauge theory can be located quickly and efficiently through the Migdal renormalization technique. Since it requires considerably less computer time, the recursion method allows surveying larger multiparameter spaces of alternative actions than those routinely accessible to Monte Carlo. Our particlar analysis is also facilitated by the study of SPCM's, as several special points (X,U,Z) and lines (XZ,ZYU) of the phase boundary lie on its intersection with SPCM planes. We may thus agree with the observation of Bachas and Dashen[11] that the topological features associated with the center Z_2 are not the unique, exclusive feature which controls the phase structure of the theory investigated.

In general, once the phase boundary of a model has been determined, it is desirable to supplement the picture by a few Monte Carlo samplings so as to specify the order of the phase transition. In the model studied here, it does not appear implausible that the entire phase boundary is first order, like its intersection with the β_F-β_A plane, a fact known from previous Monte Carlo[1] analysis. However, in our picture, part of this boundary appears as third order, in agreement with the critical exponent ν=.66 of the Z_2 limit of the theory (Q, and R of Fig. 1), as computed in the Migdal scheme[5]; the critical exponent of C is $2-\nu d \simeq -.64$.

The above critical exponent ν controls the repulsive strength of the unstable fixed point γ on the Z_2 phase transition boundary, in agreement with the pattern of renormalization flows observed in Sec. IV. One might object that since the Migdal procedure misses the order of the

transition and the critical exponents, the pattern in which the actual renormalization trajectories are affected by the phase boundary might be intrinsically different from the one observed in Sec. IV. We choose not to argue at length about the degree to which the results of Sec. IV are representative of the actual flows: we wish to simply state the features observed in the framework of the Migdal approximation, and ask whether evidence for these features can be obtained through other techniques, including Monte Carlo. Such a program appears to us well worth pursuing, considering its implications for the continuum limit.

Successive renormalizations which produce the effective theory applicable to longer distances drive all points in the space considered away from the phase boundaries and towards either the SU(2) fixed line close to the Wilson axis β_F, or else the SO(3) fixed line close to the adjoint axis β_A (Fig. 1). As a consequence, any point with sufficiently small coupling (large $1/g_0^2 = \beta_F/2+2\beta_A+5\beta_3$, viz. 2.14) at a small length scale will correspond to points on its appropriate fixed line with larger coupling at longer distance scales. For instance the points around (.65,-.06) in Fig. 8 represent physics defined equally well through: an action with (.8,.25) and a lattice spacing smaller by $1.1^{13}\simeq 3.5$, an action with (1.91,-.25) and a spacing smaller by $1.1^{20}\simeq 6.7$, or an action with (.4,.75) and a spacing smaller by $1.1^{41}\simeq 49.8$. Thus points on the fixed line represent the universal long distance behavior of the theory. Ideally, in order that the lattice spacing be much smaller than the physical object studied, the bare coupling of the theory should be defined at very large $1/g_0^2 = \beta_F/2+2\beta_A+5\beta_3$. However, practical constraints in Monte Carlo studies restrict one to relatively small $1/g_0^2$. How small can this

quantity get without losing agreement with perturbative scaling?

Let us inspect the first trajectory of Table II, which appears to join the SU(2) fixed line fairly rapidly. The effective lattice spacing after N iterations is $a_N = \lambda^N a = 1.1^N a$. The lowest order strong coupling result for the approach to the origin in the β_F-β_A plane is[3]

$$-\ln \frac{\beta_F(1+2\beta_A)}{2} \approx \sigma a^2 1.1^{2N} \qquad (5.1)$$

where N is the number of iterations (zeroed arbitrarily). Indeed, the logarithm of the l.h.s. of (5.1) evaluated at the end of this trajectory varies almost linearly with N/2, with roughly the expected slope.

In some contrast to the above, the points on the beginning portion of the same trajectory are not described as well by the perturbative scaling formula:[3]

$$-12(\beta_F+4\beta_A)+\frac{30\beta_A}{\beta_F+4\beta_A}+\frac{102}{11\pi^2}\ln(\beta_F+4\beta_A)=\frac{11}{\pi^2}\ln\Lambda^2 a_N^2 =$$
$$=\frac{11}{\pi^2}[\ln\Lambda^2a^2+2N\ln 1.1] \qquad (5.2)$$

If we consider the first ten points of trajectory 1 (x in Fig. 9), g_0^2 lies between 1.25 and 5.17, fairly large. The left hand side of (5.2) evaluated at these points does not vary exactly linearly with N, as would be expected for constant Λ. This indicates that these points are not yet in the weak coupling regime, or that Λ is not a constant.[3,1] However, the slope of an eyeball straight fit through them is only slightly higher than the slope predicted, which is a familiar feature of the β functions obtained through Migdal recursions.[5,9] For smaller couplings (e.g. $g_0^2 < .80$) on the SU(2) stable line, we find that scaling through (5.2) works quite well. (Also compare to Fig. 3 of Ref. 3,

especially for small negative β_A.) However, several other trajectories off the fixed line simply cannot be fit by (5.2), even though they cover ranges of lower couplings g_0.

We therefore consider it worthwhile to ask whether the SU(2) stable trajectory always approaches perturbative scaling faster than trajectories with comparable g_0's, a fact which may have practical applications in Monte Carlo calculations.[3,4]

It appears likely that, even beyond the framework of our approximation, the SU(2) universal line (which consists of a small negative component of adjoint action superposed to the Wilson action, $\beta_A \simeq -.16\beta_F$) furnishes the optimal pathway to the continuum limit.

It is a pleasure to thank W. Bardeen, A. Buras, D. Callaway, E. Eichten, P. Mackenzie, and S. Shenker for suggestions and criticism. We are also indebted to R. Raja for generous assistance in computing. K. M. B. further wishes to thank W. Bardeen and the Fermilab Theory Group for their hospitality.

APPENDIX A

LOCAL MINIMA OF THE SINGLE PLAQUETTE ACTION

Bachas and Dashen[11] have observed that the phase structure of lattice gauge theories in the manifold of alternative actions is often demarcated by those regions of that manifold which contain stable classical local minima of the single plaquette action, in addition to the trivial one (which corresponds to the vacuum). They speculate that excitations made up of single plaquette configurations condensed in these local minima are responsible for the discontinuous change in energy characteristic of a first order phase transition. Some, but not all, of these minima correspond to the nontrivial element in the center [Z_2 for SU(2)], which is associated with the fluxon/monopole multiplaquette configurations conjectured to govern the thermodynamics of confinement.[12] Even though this type of analysis does not anticipate the full phase structure of our system, we still find it useful in locating several nontrivial features in our phase diagram.

Our classical action:

$$S = -2\left(\beta_F \cos\theta/2 + \beta_A \cos\theta + 2\beta_3 \cos\theta \cos\theta/2\right) \quad (A.1)$$

is extremized through the condition:

$$\frac{\partial S}{\partial \theta} = 0 = 12\beta_3 \sin\frac{\theta}{2}\left(\cos\frac{\theta}{2} + \frac{\beta_A + \sqrt{\beta_A^2 + 6\beta_3(\beta_3 - \beta_F/2)}}{6\beta_3}\right)\left(\cos\frac{\theta}{2} + \frac{\beta_A - \sqrt{\beta_A^2 + 6\beta_3(\beta_3 - \beta_F/2)}}{6\beta_3}\right)$$

(A.2)

The condition for stable minima is

$$\frac{\partial^2 S}{\partial \theta^2} = \frac{\beta_F}{2}\cos\frac{\theta}{2} + 2\beta_A\cos\theta + \beta_3\left(5\cos\theta\cos\frac{\theta}{2} - 4\sin\theta\sin\frac{\theta}{2}\right) > 0 \qquad (A.3)$$

In the octant under study ($\beta_F, \beta_A, \beta_3 \geq 0$) there is always a stable minimum at the vacuum: $\theta = 0, 4\pi$. Moreover, there is always an extremum to be found at $\theta = 2\pi$, which corresponds to the nontrivial element of Z_2. However, it is a minimum only for

$$2\beta_A - \frac{\beta_F}{2} - 5\beta_3 > 0 \qquad (A.4)$$

The plane EOB of Fig. 1 defined by the equality limit of the above (A.4) leaves all center minima to its left. It intersects the β_A-β_3 plane ($\beta_F = 0$) along OE (defined by $\beta_A = 5/2\ \beta_3$); the β_A-β_F plane ($\beta_3 = 0$) along OB (defined by $\beta_F = 4\beta_A$); and the WXTS phase boundary (found to be roughly planar: $\beta_A + \beta_F + \beta_3 \simeq 1$) along XYZ (roughly: $21\beta_F + 10 \simeq 14\beta_A, \beta_3 \simeq 1 - \beta_A - \beta_F$).

We find that the triple point X of the β_A-β_3 diagram lies on the intersection of OE with the phase surface WXTS, and the well known[1] critical endpoint of the β_A-β_F diagram lies very near[11] Z, the intersection of OB with the same phase surface.

To the right of the plane EOB, the center element $\theta = 2\pi$ converts to a local maximum, which may well continue to infuence the functional integral, and be associated with the wide heat capcity bumps found along ZS.

To the right of the OE on the β_A-β_3 diagram, the minimum splits into two symmetric ones about 2π, which migrate continuously from 2π to 2 arcos $(-1/\sqrt{6})$ along

$$\theta = 2 \arccos\left(\frac{-\sqrt{6+(\beta_A/\beta_3)^2} - \beta_A/\beta_3}{6}\right) \qquad (A.5)$$

On the β_F-β_3 plane these minima migrate on with increasing β_F/β_3 along

$$\theta = 2 \arccos\left(-\sqrt{\frac{1}{6} - \frac{\beta_F}{12\beta_3}}\right) \qquad (A.6)$$

until they reach $\pm\pi$, where they vanish for $\beta_F \geq 2\beta_3$ (line OD).

The region where there can be no extrema at real angles other than 0 and 4π is determined by the argument of the square root in(A.2):

$$\beta_A^2 + 6\beta_3\left(\beta_3 - \frac{\beta_F}{2}\right) < 0 \qquad (A.7)$$

This is the interior of a slanted cone with its apex at the origin and an elliptic intersection with the β_F = constant planes:

$$\left(\frac{\beta_A}{\sqrt{6}}\right)^2 + \left(\beta_3 - \beta_F/4\right)^2 = \left(\beta_F/4\right)^2 \qquad (A.8)$$

This slanted cone is tangent to the EOB planealong the line OG defined by

$$\beta_A = 6\beta_3 \quad , \quad \beta_F = 14\,\beta_3 \qquad (A.9)$$

The phase boundary intersects the cone and this tangent along the curve UYS and the point Y [roughly: (0.65,0.30,0.05)], respectively.

Finally, the very small region bounded by GOB, BOF, and the surface of the cone does not contain local minima, since both (A.2) solutions for cos $\theta/2$ are not ≥ -1 and thus do not correspond to a real angle.

We have found no local minima structure to account for the location of the triple point W.

The minima boundaries thus found demarcate our data points quite distinctly:

a) Points inside the boundary UYZS are characterized by wide bumps - and are thought to correspond to no real boundary.

b) Points to the right of XY outside the cone correspond to remarkably sharp cusps.

c) Points on XZW are fairly narrow peaks.

APPENDIX B

ALTERNATIVE RECURSION FORMULAS

We remarked in Sec. 2 that Migdal's formula (2.5) is exact in two spacetime dimensions (d=2) for $\lambda=2$. This may be seen directly by decimating the lattice, i.e. integrating out all links which lie on alternative parallel lines of these planes, by use of (2.2). Unfortunately, this procedure cannot be extended to lattices of higher dimensionality, because the integrals do not yield local, one plaquette expressions. Migdal proposes[5] to avoid this problem by averaging over loops in adjacent planes, after decimating half the links on these planes. Thus the effective theory arises as the average of actions in adjacent planes which cover the entire lattice. In general, on a highly correlated lattice, the error introduced by this averaging should not be very large.[6]

Kadanoff[6] has proposed a variant of this prescription in which the link shifting/averaging precedes decimation. This enables him to gain some insight into the accuracy of the approximation. An effort[7] to improve these formulas systematically by incorporating the nonlocal interactions, so far projected out at every step, is too cumbersome for our numerical approach.

We generalize the recursion formula (2.5) through the introduction of a parameter b:

$$e^{-S_p(U,\lambda a)} = \left[\sum_r \left(\frac{1}{d_r}\int dV\, e^{-S_p(V,a)\lambda^b} \chi_r^*(V)\right)^{\lambda^2} d_r \chi_r(U)\right]^{\lambda^{d-2-b}} \qquad (B.1)$$

This formula interpolates between the Migdal recipe used here (b=0), and

the Kadanoff prescription (b=d-2). The exponent λ^2 continues the result obtained by decimation on a plane (λ=2). The exponents λ^b and λ^{d-2-b} result from link shifting/averaging before and after decimation respectively. One may observe that a succession of several transformations (B.1) depends on b only through the first and the last exponents in the nested parentheses of the combined transformation. We note below that the variation of our results with b is not dramatic. We do not study here successions of variations with alternating b's.

As remarked in Sec. II, a succession of two transformations with a given lattice spacing expansion factor λ is not in general equal to one with λ^2, unless λ=1. This, of course, is the reason why we iterate many transformations with a λ only slightly above 1. (Actually, λ<1 can be studied as well: through the method of Sec. IV, we observed reversed flows for λ = 1/1.10, but, naturally, the series for the free energy does not converge.)

In this study we have worked with λ=1.10, because that value reproduces the SO(3) critical coupling with the Migdal formula. Once this parameter has been chosen, no further adjustments have been made to obtain agreement with the Monte Carlo data (Fig. 5). How much would we expect the results to vary if no critical coupling were available on the outset of our study?

To discuss this question, we perform some runs on the same ray $\vec{c}$ = (.23,1,0) with variable λ and b (see Fig. 10). We note that in the Migdal recipe (b=0,Figs.10 a,b,c), the critical β and the heat capacity peaks increase with increasing λ. Even though the location of each peak varies by $\simeq$10% between λ = 1.05 and λ = 1.15, the distance between two peaks varies by less than 4% in the same λ interval. This is smaller

than the error bars for this quantity in the Monte Carlo calculation[1] at the same region.

In contrast to the above, β_c and the height of the C peaks decrease with increasing λ for the Kadanoff recursion formula (b=2,Figs.10d,e,f). Even for fairly small λ's (e.g. λ=1.03 in Fig.10f) the labile values of β_c obtained by the Kadanoff prescription are underestimated. Thus, since smaller λ's require considerably larger numbers of iterations for convergence, the Migdal formula seems preferable for our purposes.

For a given λ, the Kadanoff prescription yields lower β_c's than those obtained through the Migdal prescription. This may not be surprising, since a succession of Kadanoff transformations with a given λ is equivalent to a succession of Migdal transformations with the same λ where the initial β is scaled up by λ^{-2} (in d=4). If, after sufficiently many iterations (when the final β is very small), the final downscaling is less important than the initial upscaling, the heat capacity computed by Kadanoff's recursion would correspond to a higher Migdal β. This is in fact what is observed: all β_c's observed in the Migdal approximation exceed those obtained in the Kadanoff approximation, for the same phase transition.

One may also interpolate between the two prescriptions discussed so far, e.g. by taking b=1 (Fig.10g). Predictably, the location of both inverse couplings β_c obtained through b=1, λ=1.05 lies between those for the corresponding couplings obtained through the Migdal and the Kadanoff recipes for the same λ.

Depending on the particular demands of the problem at hand, one may adjust λ, (and even d, by a small amount) to establish contact with known results. Even if no critical couplings are available, we may

still see that the variability of such results with respect to adjusting these parameters is not too large so as to cast doubts on their reliability. For the purposes of the problem investigated here, we are led to choose the Migdal formula, since its optimal λ is reasonable in the sense that it does not require excessively long iteration sequences.

REFERENCES

[1]G. Bhanot and M. Creutz, Phys. Rev. D24 (1981) 3212. Also see:

[2]G. Bhanot, Inst. for Adv. Study preprint, December 1981; C. Lang et al., Phys. Lett. 101B (1981) 173; S. Anthony, Phys. Lett. 110B (1982) 271; J. Drouffe, Phys. Lett. 105B (1981) 46; Nucl. Phys. B205 [FS5] (1982) 27; S. Samuel, Phys. Lett. 112B (1982) 237; D. Pritchard, Phys. Lett. 106B (1981) 193.

[3]G. Bhanot and R. Dashen, Inst. for Adv. Study preprint, February, 1982.

[4]B. Grossman and S. Samuel, Rockefeller preprint, RU82/B/25, May 1982.

[5]A. Migdal,Sov. Phys. - JETP, 42 (1976) 413; ibid 743.

[6]L. Kadanoff, Ann. Phys. 100 (1976) 359. J. José et al., Phys. Rev. B16 (1977) 1217.

[7]G. Martinelli and G. Parisi, Nucl. Phys. B180 [FS2] (1981) 201.

[8]K. Wilson, Cargèse 1979 Summer School Notes, in Quarks and Leptons; M. Levy et al. eds. (Plenum, New York, 1980), p. 363.

[9]M. Nauenberg and D. Toussaint, Nucl. Phys. B190 [FS3] (1981) 217.

[10]S. Caracciolo and P. Menotti, Nucl. Phys. B180 [FS2] (1981) 428.

[11]C. Bachas and R. Dashen, Inst. for Adv. Study preprint ,March 1982.

[12]G. 't Hooft, Nucl. Phys. B138, (1978) 1; T. Yonega, Nucl. Phys. B144, (1978) 195; G. Mack and V. Petkova, Z. Phys. C12 (1982) 1977; R. Brower et al., Phys. Rev. Lett. 47 (1981) 621; R. Brower, et al., Nucl. Phys. B205 [FS5] (1982) 77; T. DeGrand and D. Toussaint, Phys. Rev. D22 (1980) 2478.

[13] J. Greensite and B. Lautrup, Phys. Rev. Lett. 47 (1981) 9.

[14] M. Creutz et al., Phys. Rev. Lett. 42 (1979) 1390.

TABLE I.

Peaks of the heat capacity $\hat{C}$ for the trial runs performed. The location of the peak (coordinates of the phase transition point) is given by ($\beta_c c_F$, $\beta_c c_A$, $\beta_c c_3$). x denotes a cusp, o a peak, and U a very wide bump. * indicates that the peak and the cusp are hard to resolve.

c_F	c_A	c_3	β_c	SHAPE	HEIGHT
0.	1.	0.	.83	o	1.75
.10	1.	0.	.82/>1.89	o/x	1.80/
.20	1.	0.	.82/>1.28	o/x	1.95/
.23	1.	0.	.81/1.17	o/x	2.00/1.75
.25	1.	0.	.81/1.08	o/x	2.10/1.82
.30	1.	0.	.81/.92	o/x	2.25/2.10
.35	1.	0.	.81/.84	o/x*	2.45
.40	1.	0.	.77	o	2.80
.42	1.	0.	.75	o	3.00
.50	1.	0.	.69	o	3.00
.75	1.	0.	.58	o	2.70
1.	1.	0.	.50	o	2.40
1.	.75	0.	.57	o	2.00
1.	.50	0.	.67	o	1.65
1.	.30	0.	.80	o	1.35
1.	.25	0.	.84	U	1.25
1.	.20	0.	.89	U	1.20
1.	.10	0.	1.02	U	1.03
0.	1.	.15	.82/1.26	o/x	2.10/2.25
0.	1.	.25	.80/.91	o/x	2.95/3.10
0.	1.	.30	.78/.82	o/x	3.55/3.70
0.	1.	.40	.72	x	5.20
0.	1.	.50	.64	x	6.40
0.	1.	1.	.46	x	9.00
0.	.50	1.	.60	x	9.50
0.	.25	1.	.73	x	13.80
0.	0.	1.	.93	x	16.50

c_F	c_A	c_3	β_c	SHAPE	HEIGHT
1.	0.	2.	.32	x	9.00
1.	0.	1.	.53	x	6.00
1.	0.	.50	.73	o	3.20
1.	0.	.25	.95	o	1.92
1.	0.	.15	1.08	U	1.47
1.	0.	.05	1.20	U	1.08
1.	1.	1.	.33	x	5.30
1.	.6	.8	.41	x	4.70
1.	.8	.6	.41	x	4.00
1.	.25	.97	.44	x	5.50
1.	.97	.25	.42	o	3.00
1.	.99	.15	.46	o	2.70
.25	1.	.25	.67	x	4.70
.20	1.	.15	.79/.81	o/x*	3.20/3.30
.15	1.	.10	.80/ 1.0	o/x	2.34/2.39
2.	1.	.50	.28	o	2.45
2.	1.30	.40	.27	x	2.50
2.	.50	.03	.41	U	1.30
1.	.10	.10	.96	U	1.40
1.	-.10	.02	>1.80	U	.80

TABLE II.

Four typical renormalization trajectories for the couplings. In each trajectory the first entry represents the initial (bare) values for the couplings, and the second entry represents the values after the first iteration; subsequently, we give the values after ΔN (2, 5, 10) successive iteration intervals. The last four points of the third trajectory have been patched in from a nearby one.

Trajectory Number; ΔN	β_F	β_A	β_3	β_4
1 ; 2	1.200	.100	0.	—
	1.256	.058	-.003	0.
	1.338	-.025	.001	-.001
	1.362	-.097	.017	-.004
	1.327	-.137	.032	-.008
	1.247	-.151	.039	-.010
	1.138	-.144	.038	-.010
	1.011	-.127	.032	-.009
	.877	-.105	.024	-.006
	.735	-.087	.016	.001
	.596	-.058	.010	-.002
	.456	-.037	.005	-.001
	.322	-.020	.002	-0.
	.201	-.007	0.	-.001
	.102	-.002	0.	-0.
	.039	-0.	-0.	-0.
	.010	-0.	0.	-0.
	.001	-0.	-0.	0.
2 ; 2	.400	.580	0.	—
	.415	.566	-.007	-.010
	.445	.518	-.019	-.021
	.471	.447	-.027	-.022
	.486	.359	-.031	-.017
	.483	.264	-.029	-.011
	.453	.169	-.020	-.004
	.391	.092	-.011	-.001
	.299	.040	-.004	-0.
	.194	.012	-.001	0.
	.101	.002	-0.	0.
	.038	-0.	0.	0.
	.009	-0.	-0.	0.
	.001	-0.	-0.	0.

Trajectory Number;	Δ N	β_F	β_A	β_3	β_4
3 ;	5	0.	.800	.800	—
		.064	.916	.829	-.032
		1.080	2.015	.895	-.395
		4.779	2.873	-.165	-.390
		5.095	2.857	-.260	-.371
		5.306	2.843	-.327	-.372
		5.514	2.819	-.395	-.370
		5.729	2.792	-.467	-.366
		5.943	2.622	-.545	-.298
		6.169	2.500	-.624	-.251
		6.403	2.389	-.705	-.209
		6.614	2.218	-.770	-.146
		6.842	2.059	-.842	-.087
		7.089	1.907	-.922	-.028
		7.328	1.720	-.994	.042
		7.600	1.543	-1.085	.116
		7.735	1.230	-1.082	.208
		7.915	.947	-1.104	.296
		8.107	.661	-1.127	.385
		8.286	.364	-1.135	.470
		8.490	.046	-1.153	.569
		8.571	-.255	-1.082	.612
		8.539	-.515	-.929	.593
		8.542	-.782	-.793	.582
		8.558	-1.067	-.653	.546
		8.498	-1.297	-.462	.515
		8.283	-1.375	-.200	.349
		8.096	-1.478	.056	.196
same (3) ;	10	7.576	-1.501	.495	-.121
		6.957	-1.388	.693	-.298
		6.314	-1.252	.732	-.353
		5.676	-1.116	.580	-.259
		5.034	-.981	.498	-.219
		4.396	-.839	.416	-.184
		3.745	-.708	.337	-.143
		3.094	-.570	.258	-.106
		2.438	-.431	.179	-.070
same(patched);	10	2.143	-.351	.135	-.050
		1.510	-.237	.081	-.026
		.817	-.097	.022	-.006
		.152	-.005	0.	-0.
4 ;	5	0.	1.100	0.	—
		0.	1.172	.001	-.035
		0.	1.484	.010	-.189
		-.001	1.564	.015	-.248
		-0.	1.485	.015	-.243
		0.	1.358	.013	-.218
		-.001	1.211	.011	-.187
		-.002	1.045	.010	-.153
		-0.	.847	.005	-.111
		0.	.599	.002	-.063
		0.	.290	0.	-.017
		0.	.042	0.	-0.
		0.	.0002	0.	-0.

FERMILAB-Pub-82/39-THY

FIGURE CAPTIONS

Fig. 1 The phase boundary surfaces in the positive $\beta_F, \beta_A, \beta_3$ octant, consistent with our trial runs.

The almost flat surface demarcated by STXW is intersected by the SPCM plane EOB along the line XZ. It also intersects the SPCM slanted cone, whose apex is at the origin, along the curve SYU. This curve is tangent to the line XZ at Y, and in fact the cone is tangent to the plane EOB along the line OYG.

The XZW portion of the surface is characterized by peaks in the specific heat, while the YXTU portion is characterized by cusps. The "window" bounded by this curve SZYU is characterized by very wide bumps in the specific heat and is believed to indicate absence of a phase boundary.

The surface XZW continues down to WXV, also characterized by peaks in the specific heat. In contrast, the surface WXRQ is defined by cusps. The points R and Q are meant to extend indefinitely out along 0A, towards the Z_2 phase transition. See Appendix A for quantitative details.

We are also depicting a typical renormalization trajectory which starts from (0,.8,.8), moves off the figure, curves back near (8.6,-1.1,-.7), and returns through the window, to reach the origin on a universal path close to the β_F axis, i.e. the Wilson action.

Fig. 2 The Free Energy per plaquette $\mathcal{F}$, for $\vec{c}=(.1,1,0)$.

Fig. 3 The average plaquette action - $\langle S_p/\beta \rangle$, for $\vec{c}=(.1,1,0)$.

Fig. 4 The heat capacity density $\mathcal{C}$ for $\vec{c}$: a) (.1,1,0), a typical peak (o); b) (0,.25,1), a typical cusp (x); c) (0,1,.15), a typical peak-cusp doublet (o/x), defining two different phase boundaries; d) (1,.25,0), illustrative of the wide bumps (U) which indicate absence of a phase boundary, predicated on the Monte Carlo results.

Fig. 5 The $\beta_3=0$ subspace of Fig.1. The dashed line represents the phase boundary obtained through Monte Carlo techniques by Ehanot and Creutz. Our scaling parameter has been adjusted to $\lambda=1.1$ so that the SO(3) transition coupling coincides with .83; no other adjustments are made. For sufficiently large β_A, the point Q demarcates the Z_2 phase transition. The point S represents the location of the heat capacity peak of the Wilson action, and it lies on the continuation of the first order phase boundary WZ. The critical point Z lies very near the SPCM line OB.

Fig. 6 The $\beta_F=0$ subspace of Fig.1. The phase boundary resembles that of Fig. 5, except that here there is no window: the phase surface continues all the way to T on the spin 3/2 axis. For large β_A the point R represents the Z_2 critical coupling predicted by self-duality. To the right of the line OE, the center is not involved in the SPCM's.

Fig. 7 The $\beta_A=0$ subspace of Fig. 1. The phase boundary terminates at or near U, on the SPCM line OD, so that SU represents part of the window on the boundary surface, and corresponds to ZS of

Fig. 5.

Fig. 8 The renormalization trajectories which start on the $\beta_3=0$ plane of Fig. 5, projected onto that plane. The trajectories curve around the phase boundary and are driven to their appropriate stable fixed line: the Major [SU(2)] fixed line has slope ~ -.16, while the Minor [SO(3)] fixed line is pretty much aligned to the β_A axis. The trajectory starting in the apparently isolated phase bounded by VW and WQ does not in fact cross the phase boundary. Instead, it develops a substantial component of spin 2, and curves around to join the adjoint axis for β_A's smaller than $\simeq$ .80.

Fig. 9 The evolution of the effective couplings $\beta_F, \beta_A \times 10$, and $\beta_3 \times 10$ versus inte ration number N, for the three trajectories starting at $(\beta_F, \beta_A, \beta_3)$: (1.2,.1,0) ×, (1.5,0,0) o , and (.8,.25,0)•,respectively. Coalescence of all β_3 components occurs at a scale too small to depict. The large N behavior is consistent with the strong coupling result, while the roughly straight portions of β_F and $\beta_A \times 10$ exhibit approximate perturbative scaling - see Sec. 5.

Fig. 10 $\tilde{c}$ versus β for $\vec{c}=(.23,1,0)$ and varying recursion step parameters b and λ. The critical inverse couplings β_c are specified for each case. a) b=0, λ=1.05; b) b=0, λ=1.10: this is the Migdal prescription used consistently throughout this work; c) b=0, λ=1.15; d) b=2, λ=1.03; e) b=2, λ=1.05; f) b=2, λ=1.10; g) b=1, λ=1.05. Note that the vertical scale is compressed in Figs. b) and c).

Fig. 1

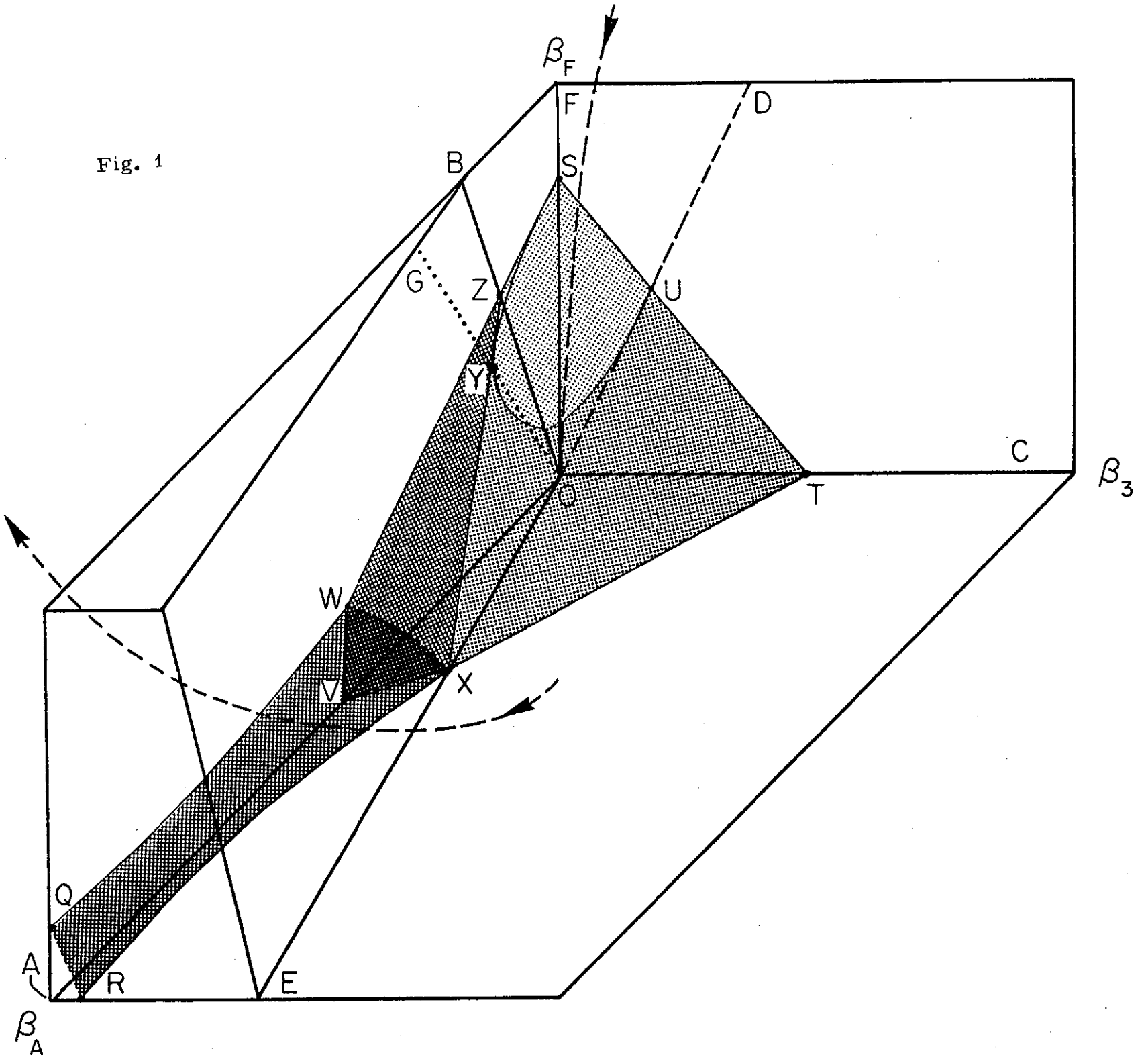

Fig. 2

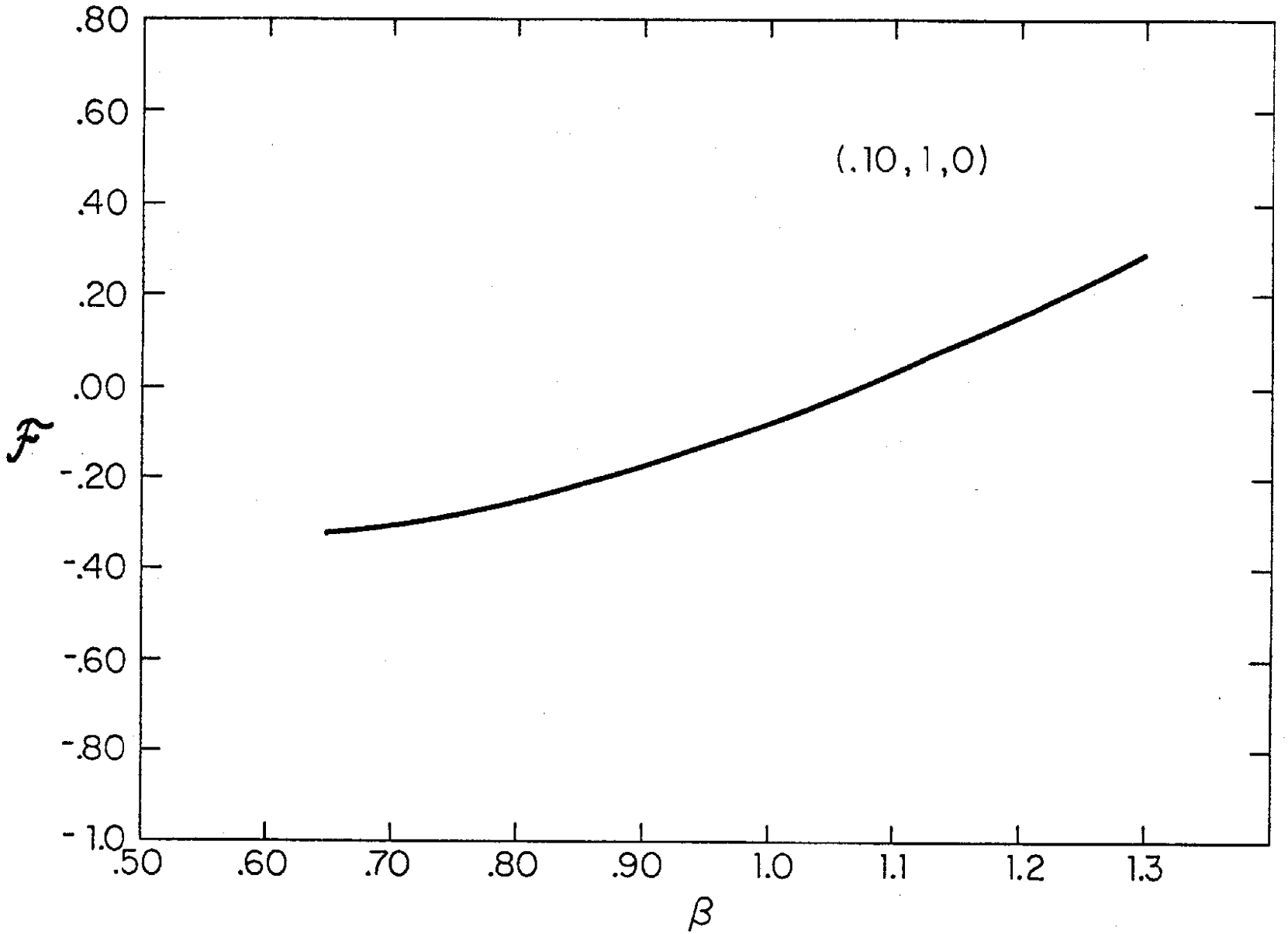

Fig. 3

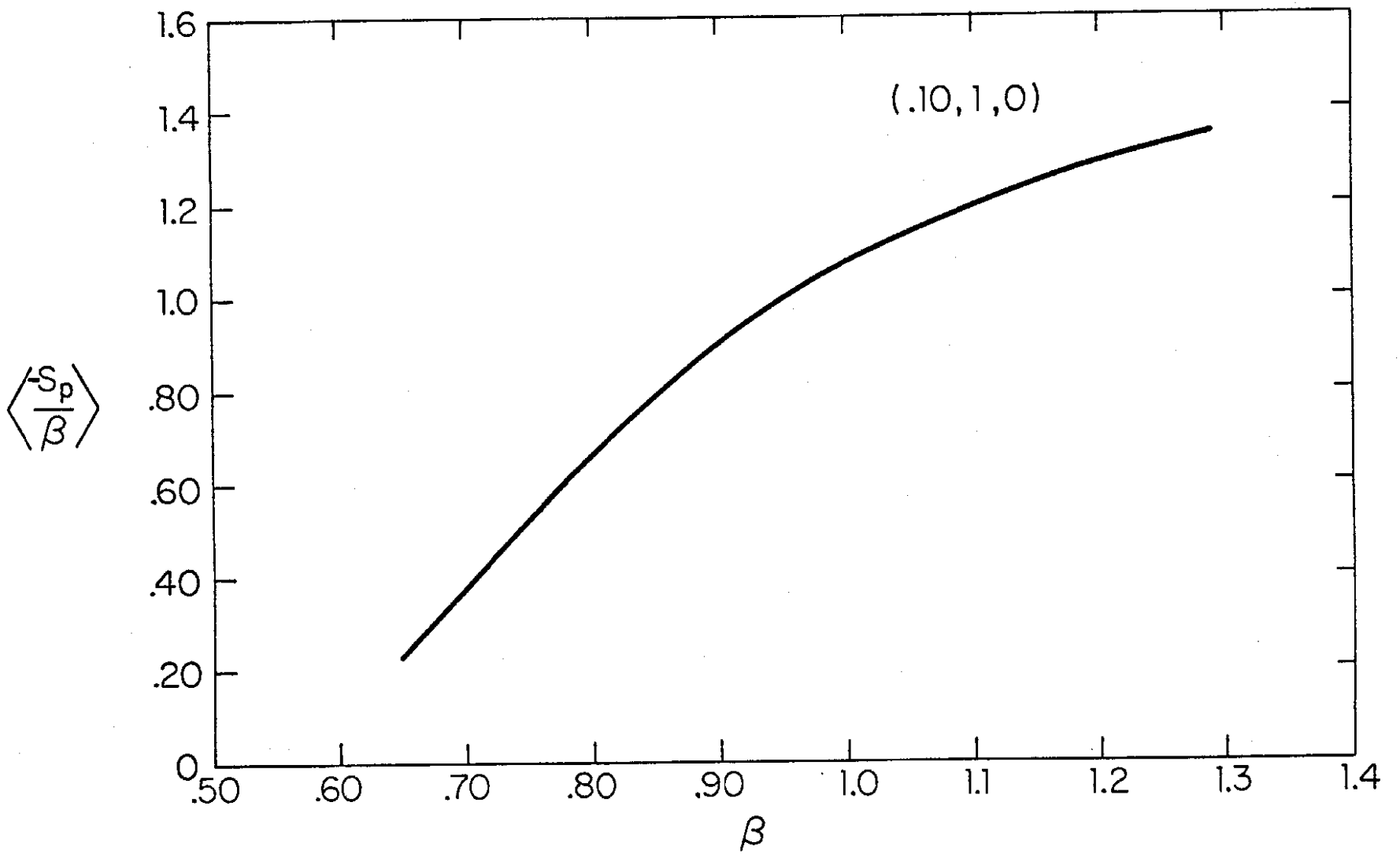
(.10, 1, 0)
$\left\langle \frac{S_p}{\beta} \right\rangle$
1.6
1.4
1.2
1.0
.80
.60
.40
.20
0
.50
.60
.70
.80
.90
1.0
1.1
1.2
1.3
1.4
β

Fig. 4a

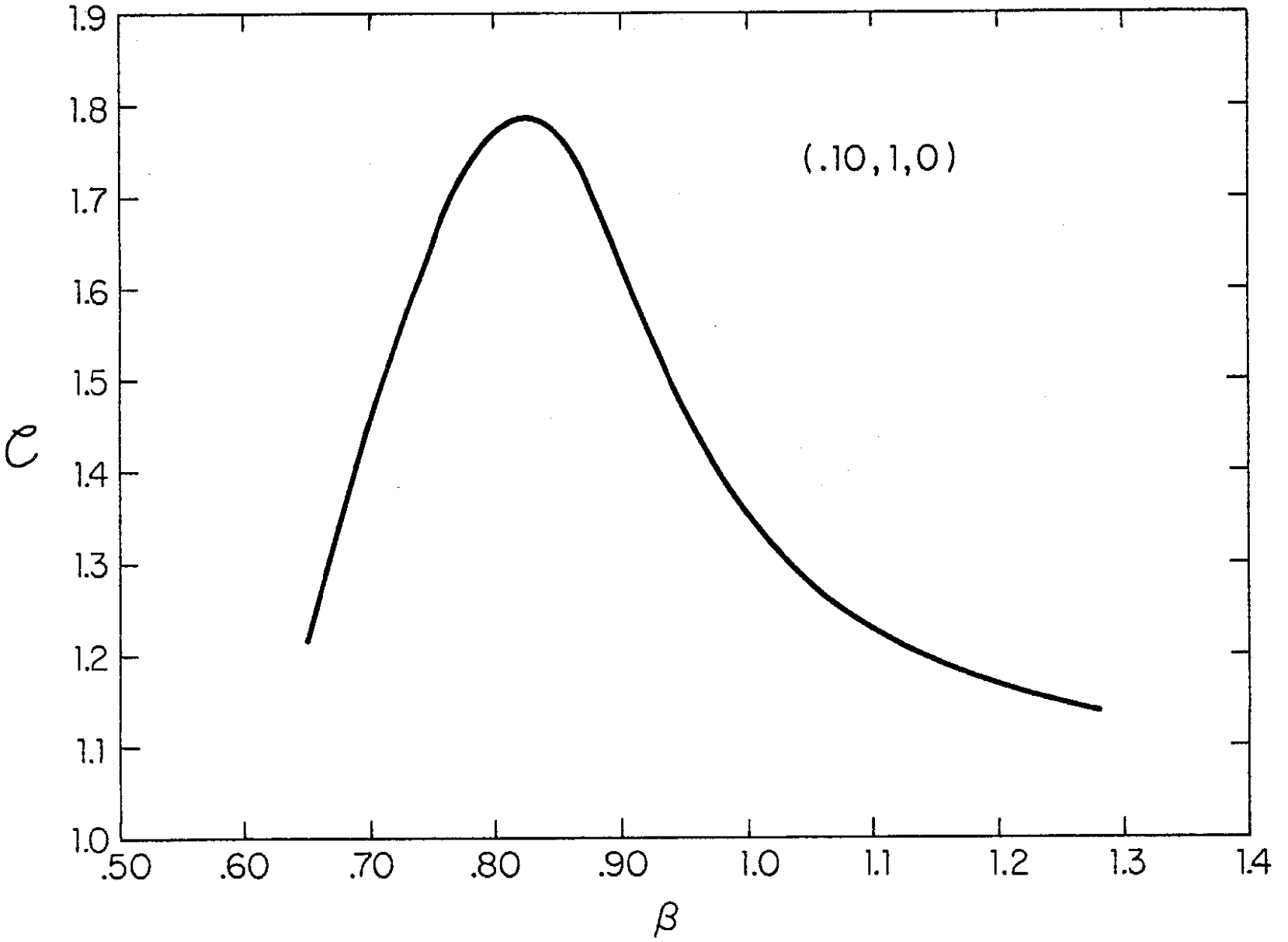

Fig. 4b

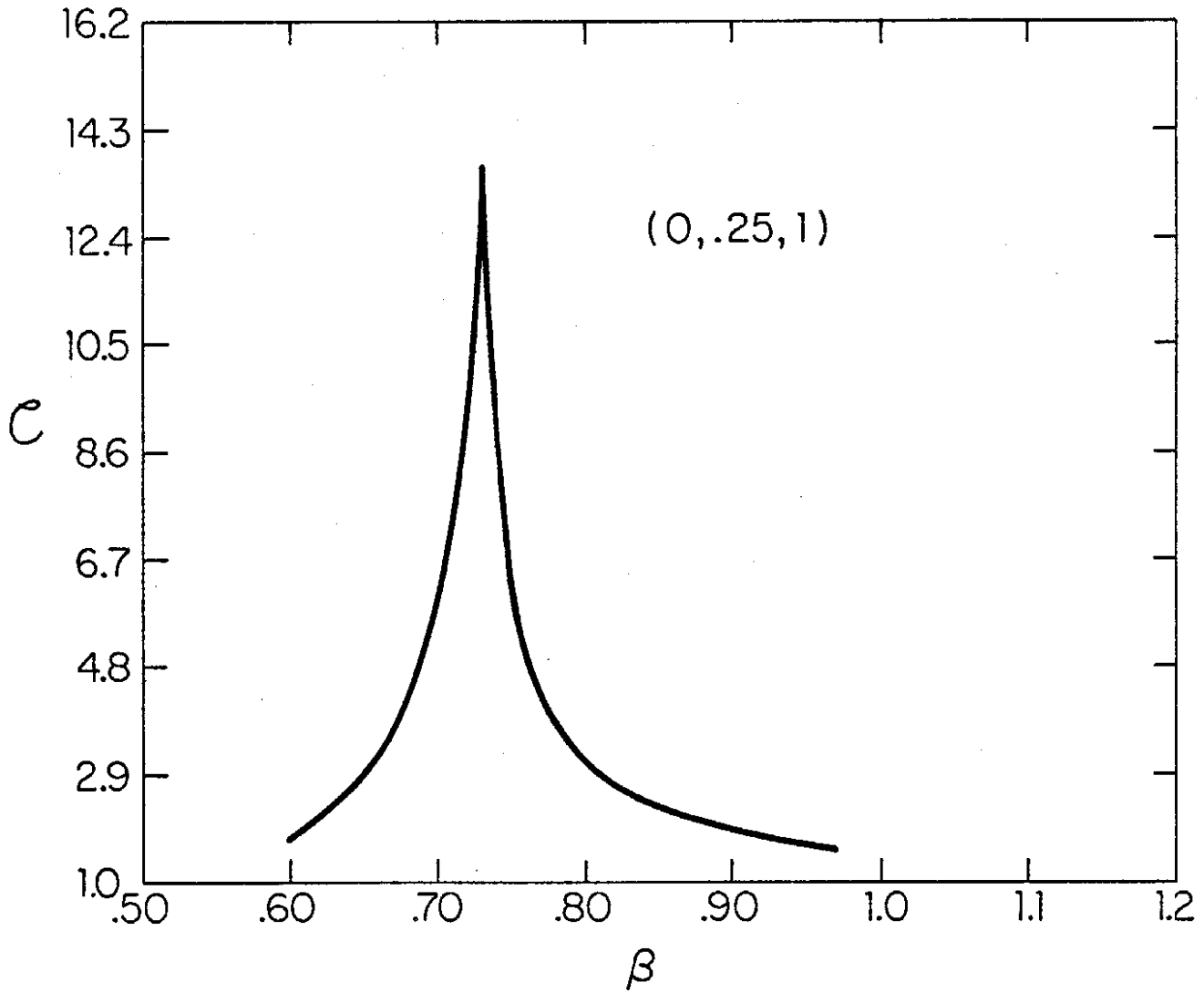

Fig. 4c

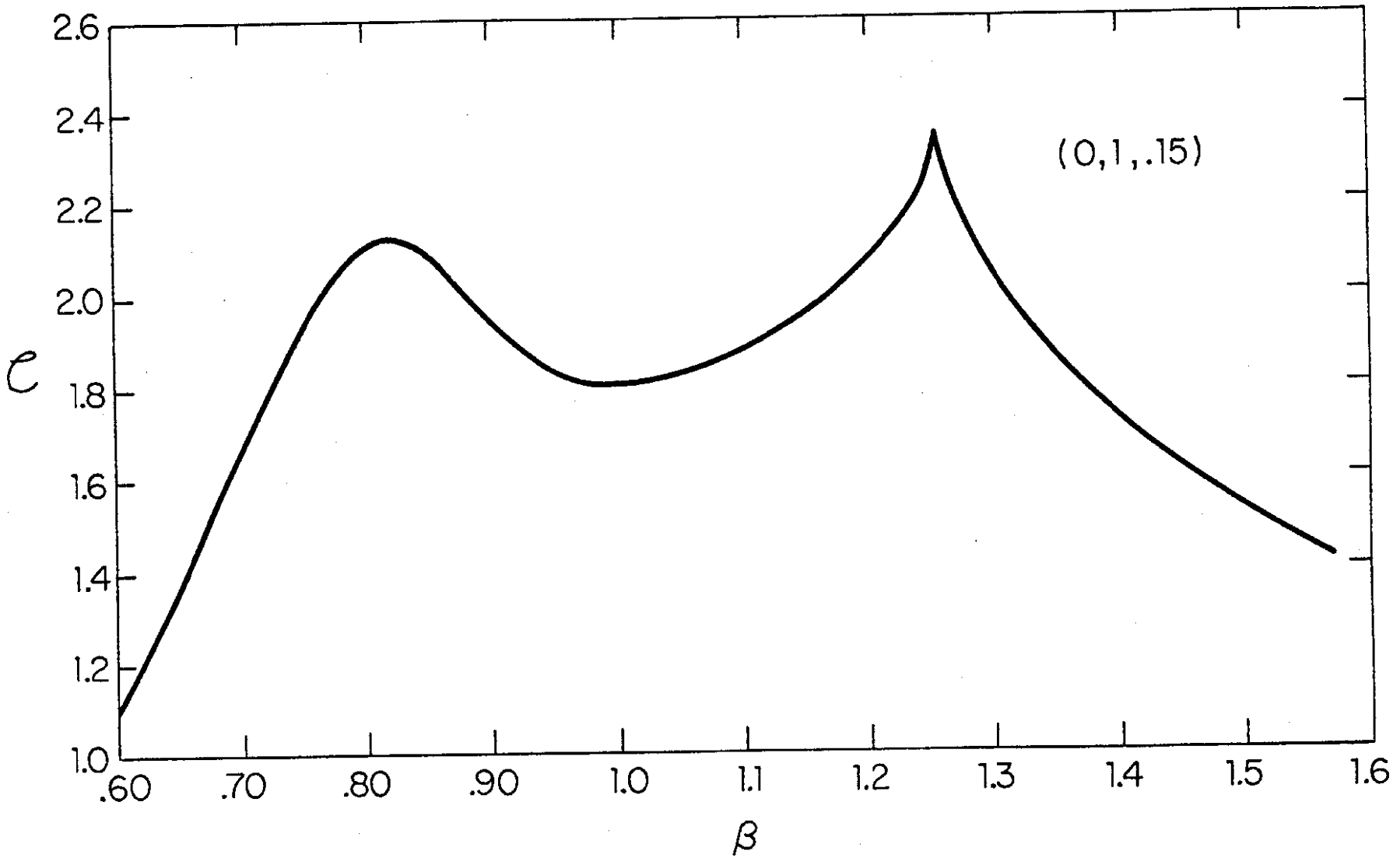

Fig. 4d

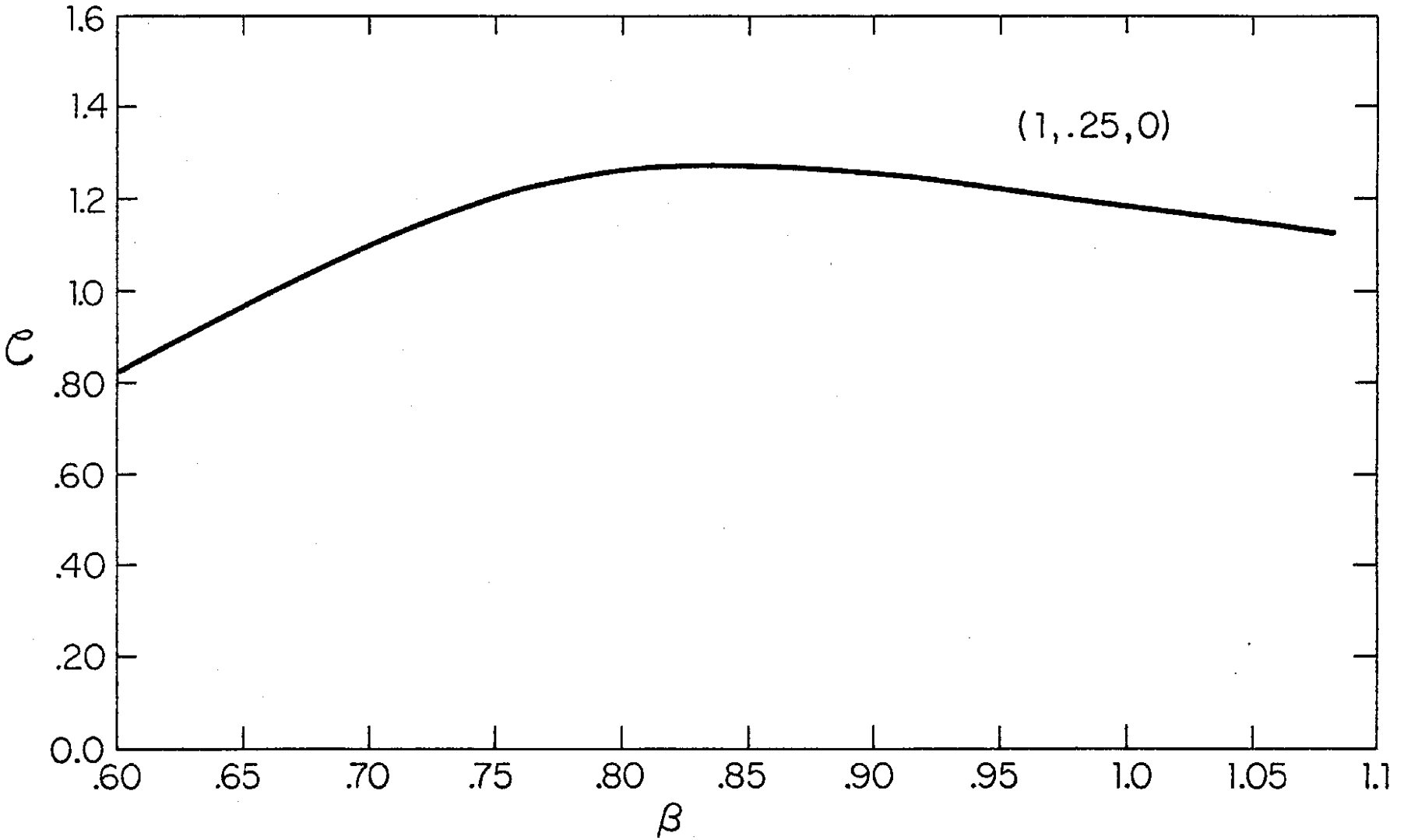

Fig. 5

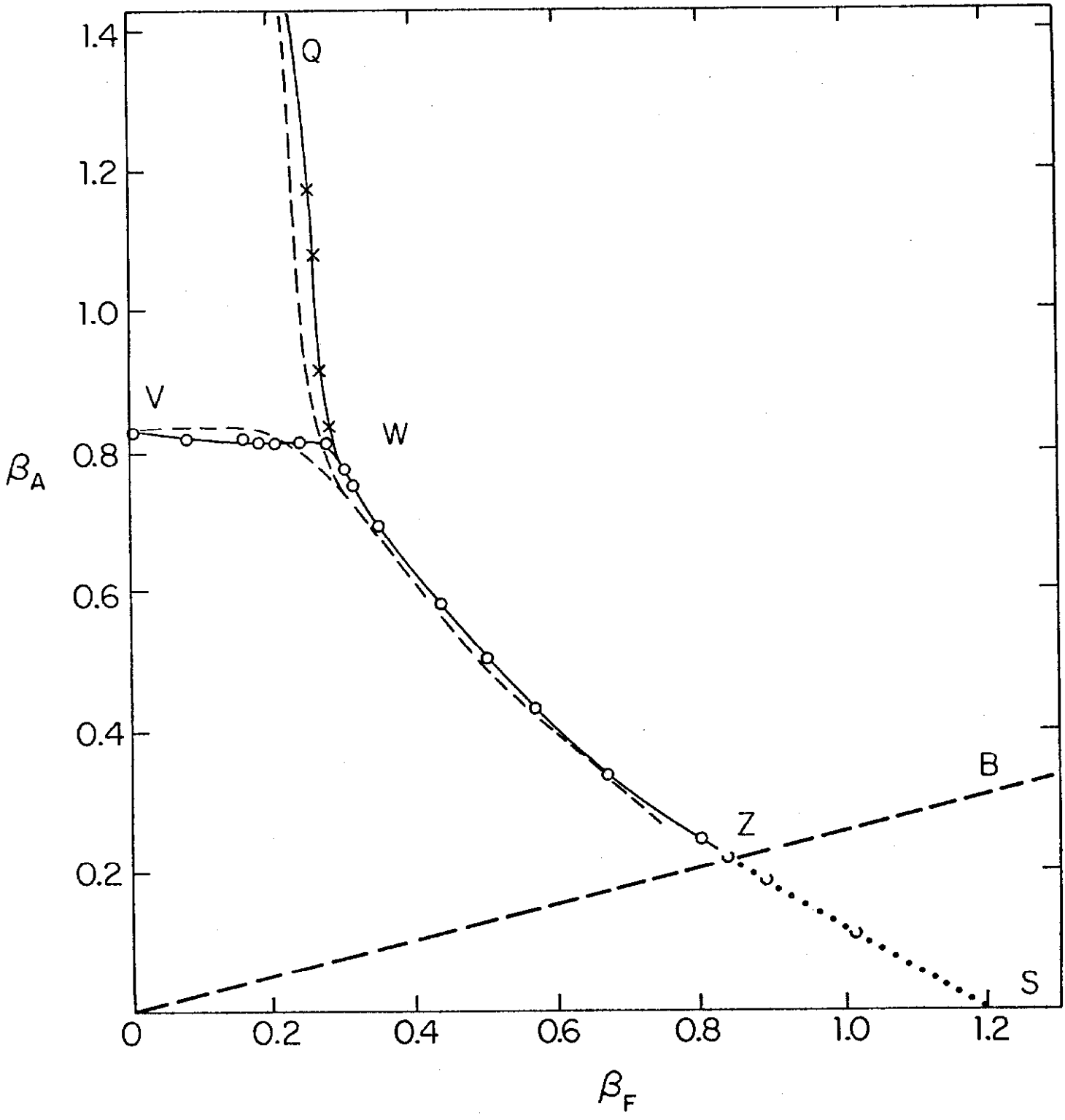

Fig. 6

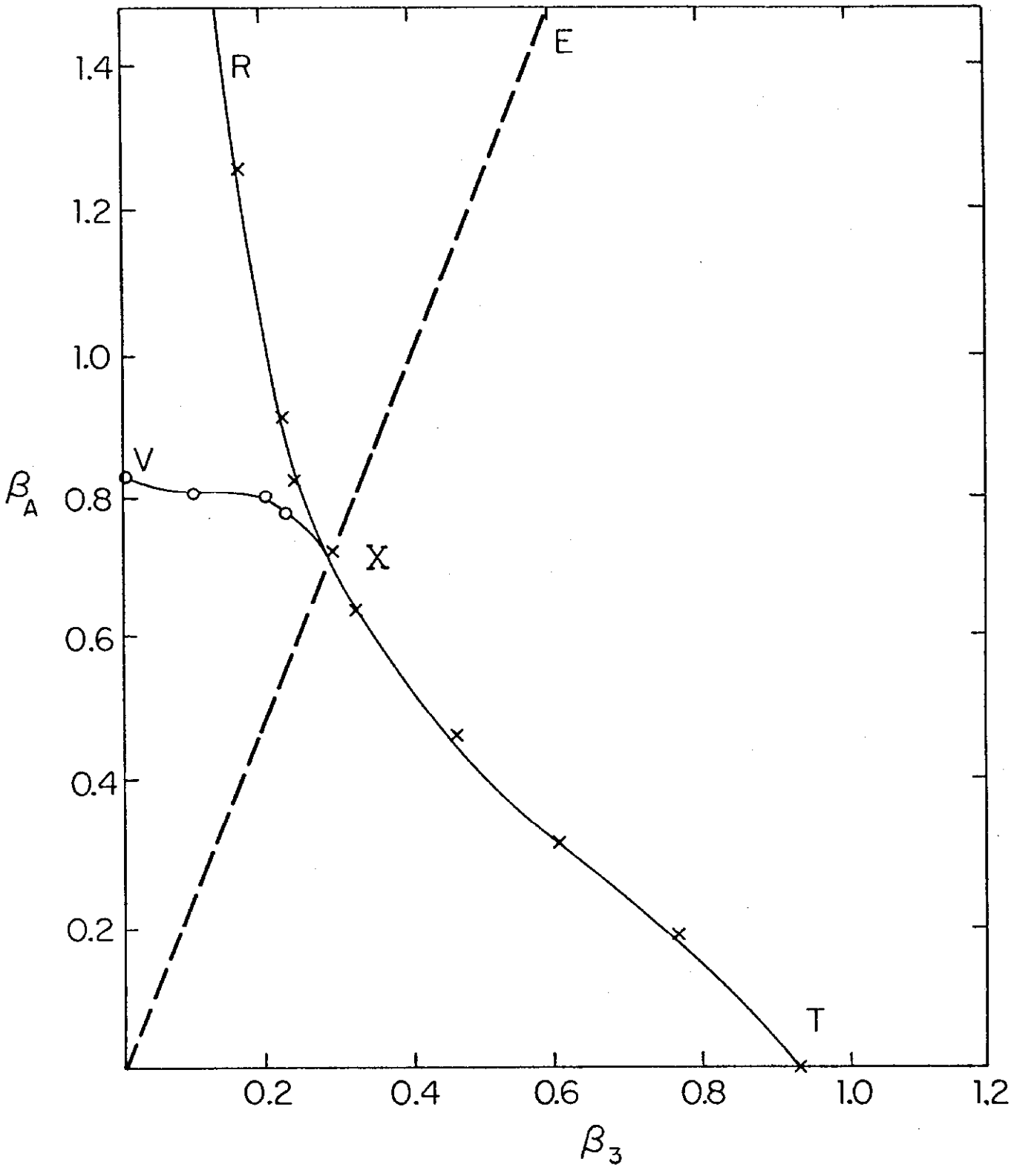

Fig. 7

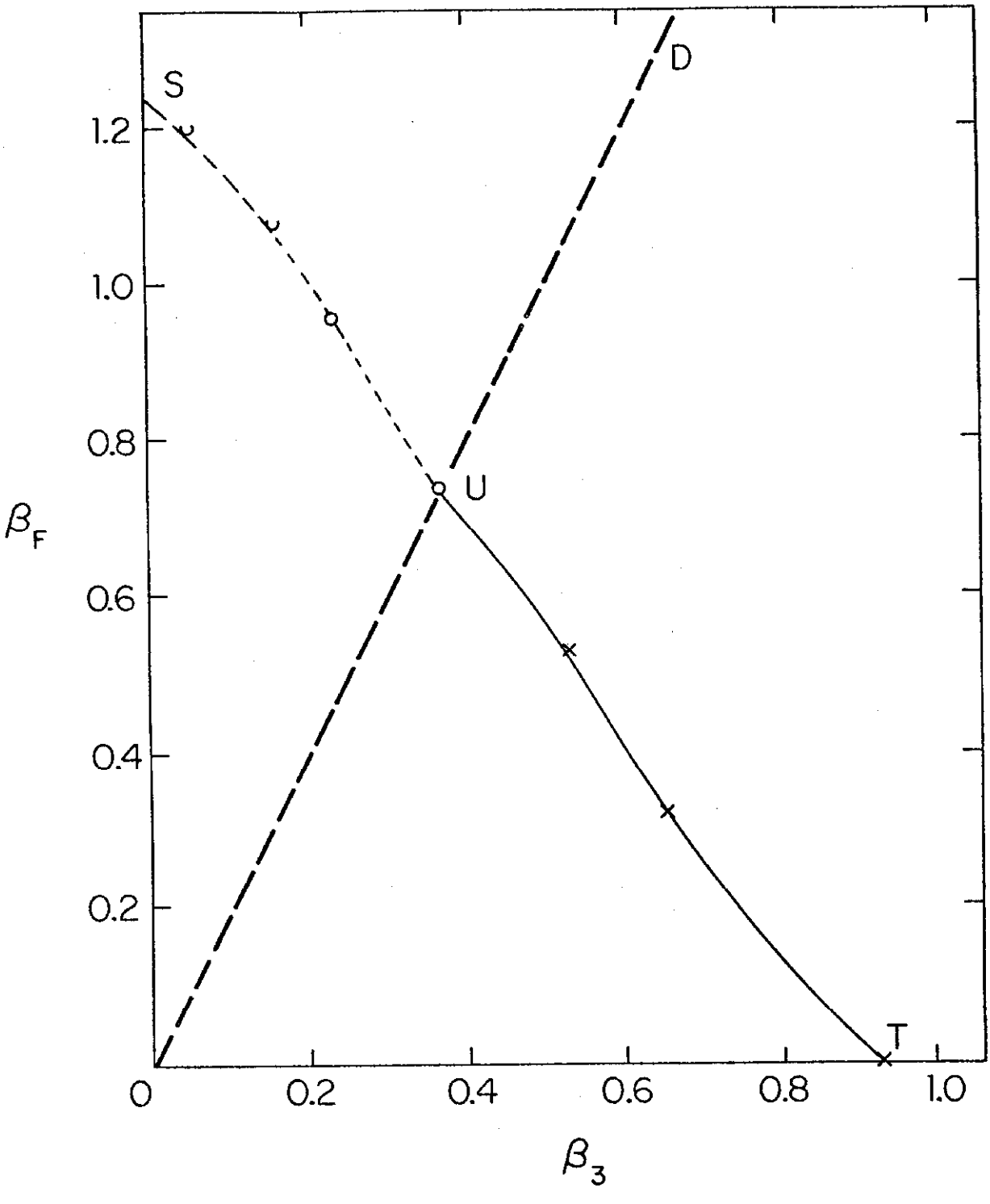

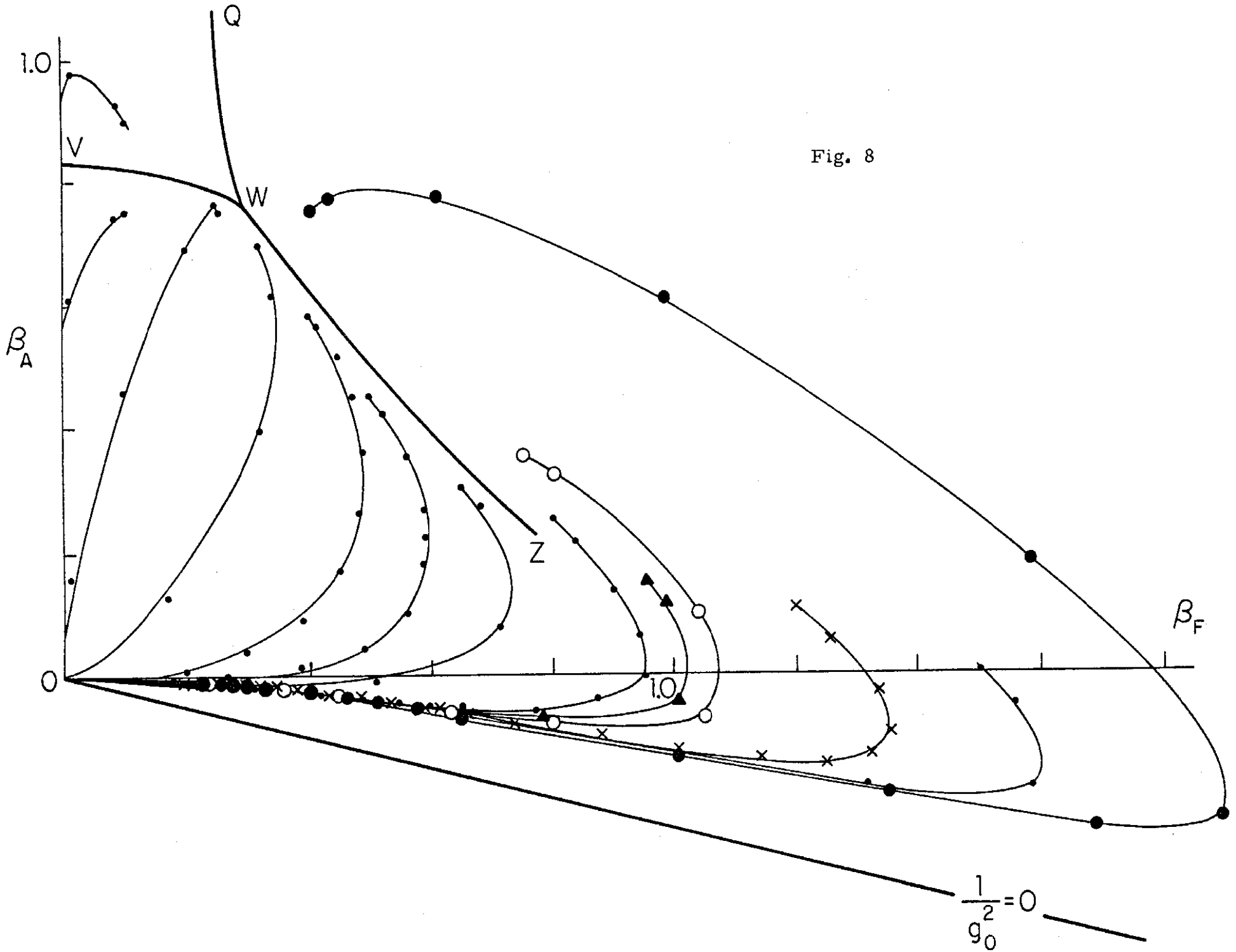

Fig. 8

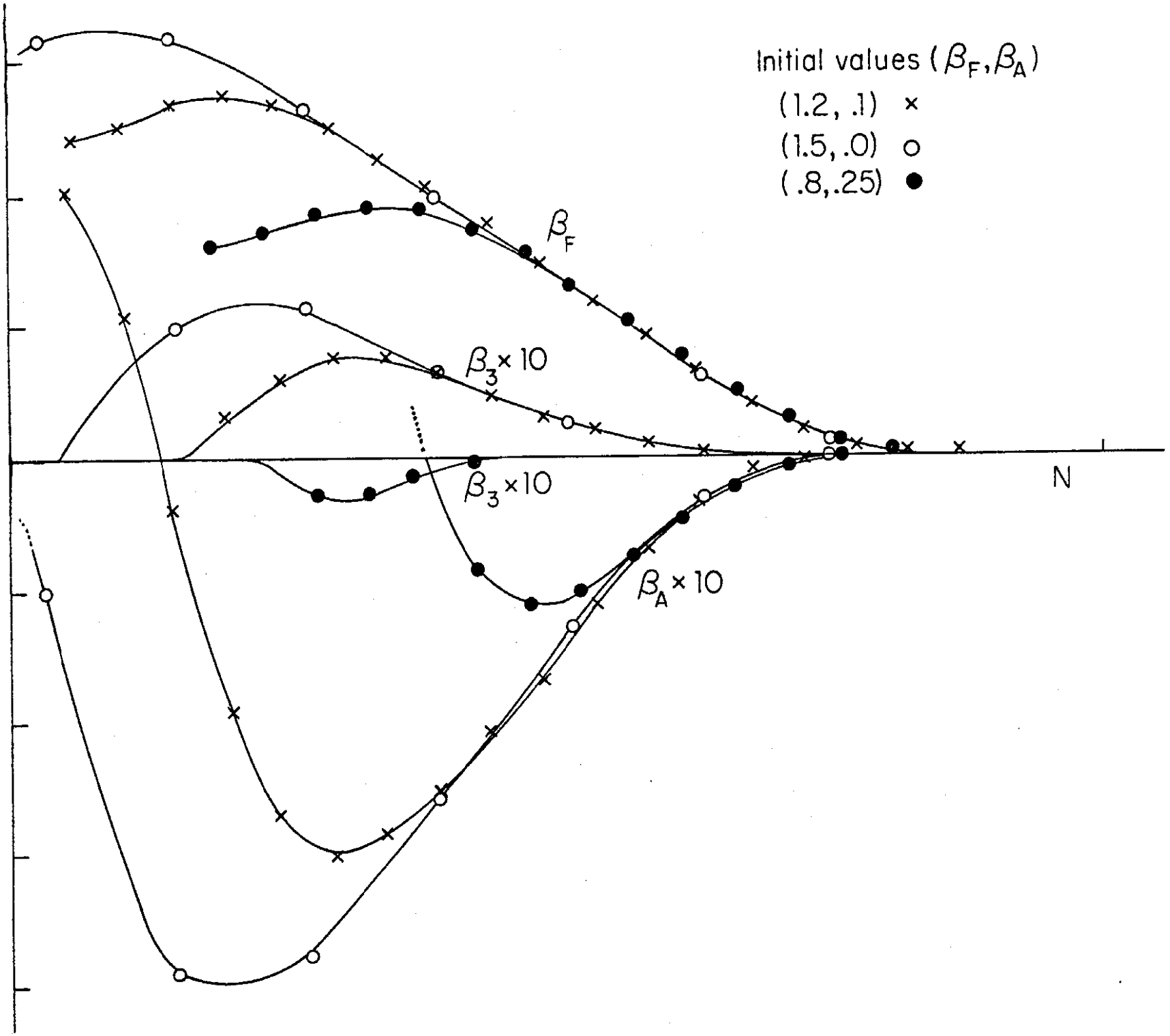
Initial values (β_F, β_A)
(1.2, .1) ×
(1.5, .0) ○
(.8, .25) ●
β_F
$\beta_3 \times 10$
$\beta_3 \times 10$
$\beta_A \times 10$
N

Fig. 10a

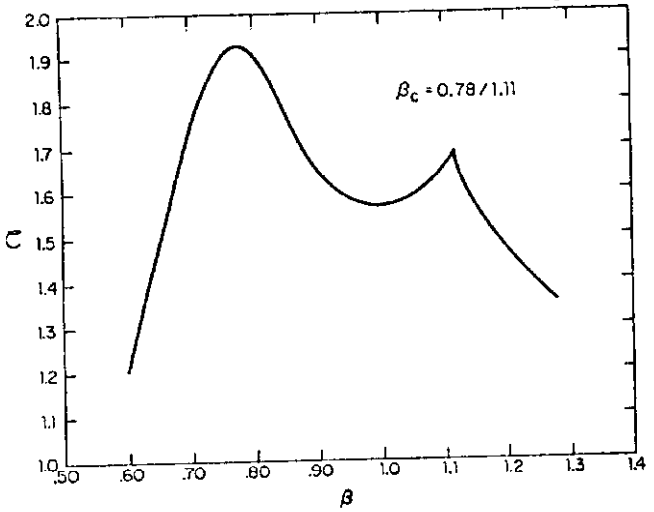

Fig. 10b

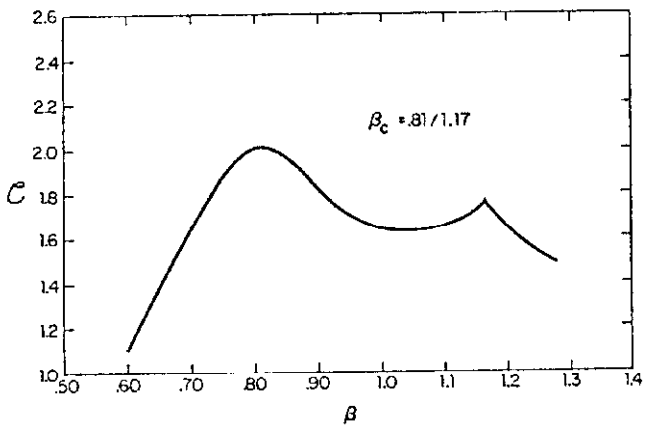

Fig. 10c

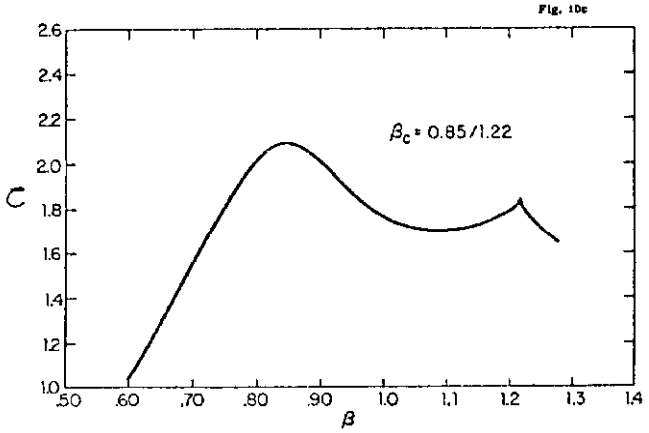

Fig. 10d

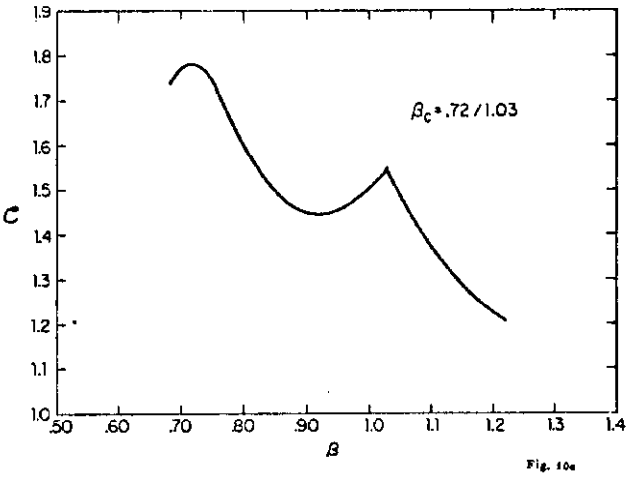

Fig. 10e

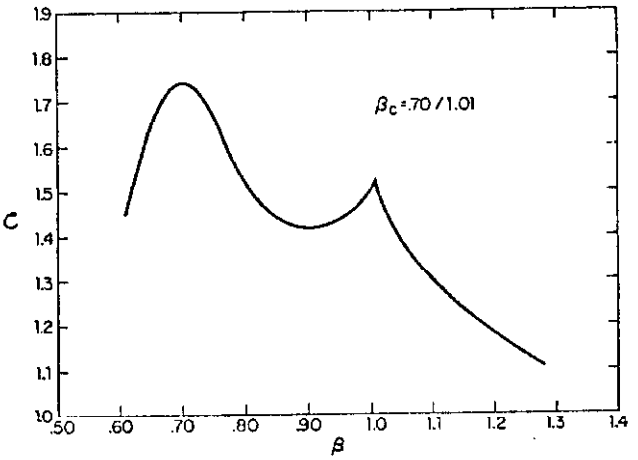

Fig. 10f

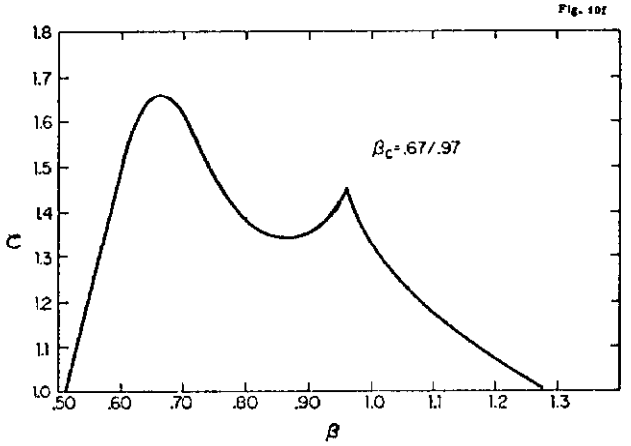

Fig. 10g